1990

The role of twin boundary and alpha prime martensite in corrosion fatigue of AISI 304 stainless steel

Shuchun Chen
Lehigh University

THE ROLE OF TWIN BOUNDARY AND ALPHA PRIME MARTENSITE IN CORROSION FATIGUE OF AISI 304 STAINLESS STEEL

BY

SHUCHUN CHEN

A THESIS

PRESENTED TO THE GRADUATE COMMITTEE

OF LEHIGH UNIVERSITY

IN CANDIDACY FOR THE DEGREE OF

MASTER OF SCIENCE

IN

DEPARTMENT OF MATERIALS SCIENCE AND ENGINEERING

LEHIGH UNIVERSITY

FALL 1990

Approved and recommended for acceptance as a thesis in partial fulfillment of the requirements for the degree of Master of Science in Materials Science and Engineering.

Dec. 13, 1990

(Date)

R . P . Wei, Professor in charge

R . W . Hertzberg, Chairman

Accepted 12/17/90

(Date)

Acknowledgement

The author expresses his sincere appreciation to Professor Robert P. Wei, his thesis advisor, for his support and guidance in the course of this graduate study. Appreciation is expressed specially to Dr. Ming Gao for his advice and assistance in this research program.

The technical assistance of Mr. C. D. Miller is greatly appreciated. Appreciation is offered to Mrs. Simmons and Mrs. Wei for their patient assistance in improving his English skills during this program. Suggestions and discussions from his fellow senior graduate students: Dr. J. P. Thomas, Dr. H. Yin and Mr. J. B. Boodey are appreciated.

Special appreciation is expressed to his wife, Ms. Minxia Liu for her understanding, encouragement and support.

The author acknowledges the State Education Committee of the People's Republic of China and The Li Foundation, Inc. (New York) for their two-year fellowship support and the financial support by the Office of Basic Energy Sciences, Department of Energy.

TABLE OF CONTENTS

List of Figures

List of Tables

Abstract

The main objective of this thesis is to define the role of twin boundary and martensitic transformation in corrosion fatigue crack growth of annealed and cold-rolled 304 stainless steels. To assist in the understanding of micromechanisms for corrosion fatigue crack growth in these steels, the relationships between the crack paths and the underlying microstructure were investigated. Corrosion fatigue in the deleterious environments (0.6M NaCl and air) was brittle, and occurred primarily by $\{001\}_\gamma$, and other unidentified, quasi-cleavage, accompanied by preferential cracking along $\{111\}_\gamma$ twin and grain boundaries. In contrast, fatigue cracking in vacuum was ductile, fully transgranular and noncrystallographic. Transformation to alpha prime(α'-) martensite by fatigue was found to be essentially complete in the cold-rolled steel, and in the annealed steel, tested in vacuum, but was substantially less in the annealed steel, tested in air and 0.6M NaCl solution. These results, taken in conjunction with the crack growth and electrochemical reaction data, support hydrogen embrittlement as the mechanism for corrosion fatigue crack growth in 304 stainless steels in 0.6M NaCl solution. Martensitic transformation is not necessary for embrittlement and is incidental to corrosion fatigue crack growth in these steels.

Chapter 1 : INTRODUCTION

This research was undertaken to assist in understanding the micromechanisms for corrosion fatigue crack growth in the metastable austenitic stainless steels. Specifically, the relationship between the crack paths and the underlying microstructure was examined for corrosion fatigue cracks in annealed and cold-rolled AISI 304 stainless steels tested by Allision [1]. Allision [1] investigated chemical and crack geometry effects on corrosion fatigue cracking of annealed and cold-rolled (25%) AISI 304 stainless steel in deaerated 0.6M NaCl solution, as well as in air and in vacuum, under constant cyclic stress intensity(ΔK) conditions. The role of microstructure on corrosion fatigue crack growth, however, was not investigated[1].

This research was initiated and was motivated by the following observations:

(1) fracture surfaces produced by corrosion fatigue crack growth in 0.6M NaCl solution and in air showed well defined, light-reflective facets and "brittle-appearing" quasi-cleavage;

(2) fracture surfaces in vacumm was ductile in nature; and

(3) fracture surfaces showed evidence of phase transformation.

Fractographic and crystallographic techniques have been used extensively to study the micromechanisms for the sustained-load cracking (or stress corrosion cracking) in austenitic stainless steels [2-5]. Comparable studies of corrosion fatigue crack growth, on the other hand, have been limited. The strain induced phase transformation during fatigue of AISI 304 stainless steel in air, hydrogen and vacuum has been demonstrated[6−8]. The formation of deformation induced martensite has been shown to increase the susceptibility to hydrogen embrittlement[9]; hydrogen appearing in many cases to first induce the transformation to martensite and then embrittling it[9]. Detailed analysis of the crack path in relation to the microstructure, however, was not done.

To understand the effect of microstructure on corrosion fatigue crack growth in AISI 304 stainless steels, metallographic, fractographic and crystallographic techniques were used in this study to identify the cracking elements and their corresponding microstructures. The role of individual cracking elements, including cyclic-load induced alpha prime martensite, was evaluated with the aid of a superposition model[10].

The thesis is organized into the following six(6) chapters: Chapter 1 is an introduction to this research; Chapter 2 contains a review of technical background; Chapter 3 provides a description of the material and experimental work; Chapter 4 describes the experimental results; Chapter 5 includes the discussions of the results; and Chapter 6 gives a summary of the research.

Chapter 2 : TECHNICAL BACKGROUND

This chapter provides the basic technical background for the understanding of corrosion fatigue crack growth in terms of the material (or microstructural) response in austenitic stainless steels. The material response is described in term of the crack path or the elemental cracking process. The cracking element is classified as being either transgranular (through a grain or along an internal interface) or intergranular (along a grain boundary). The detailed fracture surface morphologies are then explained in relation to the fracture processes.

2.1 Review of fractographic analyses

The fractographic features of stress corrosion cracks in austenitic stainless steels were well investigated [2-5]. More attention was paid to the crystallographic orientations of the microfractographic features. Meletis et al. [11] summarized the crystallographic methods for small-facet orientation determination. Liu et al. [3] employed photogrammetric and electron channelling techniques to show that the fracture facets corresponded to {100} planes in 310 stainless steel. The situation was more complicated for 304 stainless steel, possibly because of the presence of martensite on the fracture surfaces. Their results indicated the presence of {110} and {211} fracture facets[3]. Mukai et al. [5], using an etch-pitting method, found that the fracture facets in 304 stainless steel cracked in boiling $MgCl_2$ solution generally corresponded to {100}, with crack growth in the <110> direction. In 304L stainless steel, Meletis and Hochmann [4,11], using etch-pitting, electron channelling, two surface analysis and photogrammetry, found predominantly {100} facets, with some {110} facets also present.

Unfortunately these investigations[2-5, 11] only identified the orientation of the fracture facets and did not investigated the corresponding microstructure. The material adjacent to the fracture facet needs to be identified either as austenitic or martensitic phase. The role of the fracture facets in determining the stress corrosion cracking growth rate also was not investigated.

2.2 Martensitic transformation

In metastable austenitic stainless steels, strain induced alpha prime(α') martensite which forms along the path of crack propagation, can play an important role both in hydrogen embrittlement[12−14] and in stress corrosion cracking[15]. But little work has been done to investigate the role of martensitic transformation in corrosion fatigue crack growth. A brief review of martensitic transformation in the stainless steel is given in the following subsections.

2.2.1 Thermally induced martensitic transformation

Reed [16] investigated the phase transformation sequence of Fe18Cr8Ni stainless steel on cooling. He found the sequence is from the γ phase to ϵ and α' martensites. The morphology of α' martensite is long, narrow plates, and these plates were bounded by $\{111\}_\gamma$ sheets. The long direction of the plates was parallel, or nearly parallel, to $<110>_\gamma$. If they were parallel to $<110>_\gamma$ then the plates had $\{225\}_\gamma$ habit planes. If they deviated from $<110>_\gamma$ then the habit plane was not $\{225\}_\gamma$. Breedis et al. [17] studied Fe16Cr12Ni austenitic stainless steel single crystals. The same sequence of transformation was observed; i.e., from the FCC γ phase to the HCP ϵ phase then to the BCC α' martensite. These studies show that the ϵ phase is the intermediate phase in the transformation of austenite to α' martensite.

In summary, the important points from the papers of Reed and Breedis for this study are as follows:

(1) Alpha prime martensite is in the form of long, narrow plates.

(2) Epsilon phase is the intermediate phase in the transformation from austenite to α' martensite. This suggests that if the material already contains epsilon martensite, it would be easier to transform to alpha prime martensite. The crystallographic and morphological information may be used for fracture components identification.

2.2.2 Strain and hydrogen induced martensite transformation

When AISI 304 stainless steel was deformed at room temperature, there was transformation of the austenite phase to α' martensite. Powell et al. [18] showed that, for uniaxial tension and compression at moderately high strain rates, the amount of martensite decreased with increasing rate. The stress assisted transformation product is identical to thermally induced martensite. Hecker et al. [19] found the martensitic transformation saturated at about 85 volume percent of α' martensite in AISI 304 stainless steel. The kinetics of the strain induced transformation was studied by Olson and Cohen[20]. The kinetics indicated that the amount of α' martensite depended on the plastic strain, which is affected in turn by stacking fault energy and strain rate.

Hydrogen induced martensitic transformation in AISI 304 austenite stainless steel was reported by Holzworth et al. [21]. Martensites induced by cathodic charging hydrogen into 304L steel were found to be the same as those formed by strain induced transformation. Hydrogen expanded the austenite lattice and lowered the stacking fault energy of austenite. The only difference between martensitic transformation induced by hydrogen absorption and that by mechnical deformation was in the ratio of ϵ martensite to α' martensite; being much higher in the hydrogen charged material.

In summary, the major points are:

(1) Strain and hydrogen induced martensitic transformation follow the same sequence FCC (γ) to HCP (ϵ) to BCC(α').

(2) Factors that lower the stacking fault energy of the austenitic phase will increase phase transformation, especially to the epsilon phase.

(3) Martensitic transformation saturated at volume fraction of about 85% alpha prime martensite in AISI 304 stainless steel.

2.3 The effect of martensite on hydrogen embrittlement

The effect of pre-existing martensite on hydrogen embrittlement was investigated by Hanninen et al. [22]. When the amount of pre-existing α' martensite

was increased, the fracture surface features became smaller and less crystallographic. At 23 vol% α' martensite, the fracture surface was characterized essentially by quasi-cleavage. Pre-existing α' martensite can increase markedly the embrittling effect of hydrogen. Briant[9] claimed that the formation of deformation induced martensite in low yield strength austenitic stainless steels greatly increased their susceptibility to hydrogen cracking. On the other hand, hydrogen embrittlement has been observed in the absence of detectable alpha prime martensite[23], and no alpha prime martensite was found on the stress corrosion fracture surfaces formed in boiling $MgCl_2$ solution [24].

The literature on the effect of dissolved hydrogen on strain induced martensite transformation is inconclusive. West et al. [25] reported x-ray data that suggested hydrogen assisted α' martensitic transformation in hydrogen charged AISI 304 stainless steel specimen strained in tension. Caskey [26], on the other hand, pointed out that dissolved hydrogen in austenitic stainless steels had little effect on strain-induced martensite transformation during room temperature deformation, but suppressed the transformation at subzero temperatures. Caskey [27] also claimed that strain induced martensite was neither necessary nor sufficient for hydrogen damage in austenite stainless steels.

In summary, the main points are:

(1) Although martensitic transformation increased the susceptibility of stainless steels to hydrogen embrittlement, it is not necessary for the embrittlement in metastable stainless steels by hydrogen.

(2) Hydrogen may have an effect on strain-induced martensitic transformation under certain circumstances.

(3) Little information, however, appears to have been reported about possible effects of martensitic transformation on corrosion fatigue crack growth in 304 stainless steels.

2.4 Outstanding issues

To further understand the role of microstructure in corrosion fatigue of 304 stainless steels, the following issues need to be addressed :

(1) the crystallographic orientation of facets,

(2) the microstructure corresponding to the fracture facet,

(3) the role of facet (corresponding microstructure) in corrosion fatigue crack growth, and

(4) the role of α' martensite transformation in corrosion fatigue crack growth.

In order to address the above issues, metallographic and crystallographic techniques will be used. A superposition model will be employed to evaluate the role of α' martensitic transformation in corrosion fatigue crack growth of AISI 304 stainless steel.

Chapter 3 : MATERIALS AND EXPERIMENTAL WORK

3.1 Material

Solution-annealed and cold-rolled AISI 304 stainless steels were used in this investigation. The chemical compositions and room temperature tensile properties of these steels are given in Table I and Table II.

3.2 Metallographic analysis

In order to reveal the microstructures of annealed and cold-rolled materials, traditional metallographic methods such as grinding, polishing and etching, were used. Electrolytic etching was used for AISI 304 stainless steel. Etching was carried out in an 10% oxalic aqueous solution at 6 volts for 60 to 90 seconds. Polarized light illumination was used to enhance microstructural contrast. The grain size of annealed material was measured by the three circle method. The microstructure was also examined by transmission electron microscopy (TEM). TEM foils were prepared by electropolishing the specimens in a 20% perchloric acid-ethanol solution at 20 volts(40 mA) and -40^{o} C. The temperature is very critical for producing a uniformly thin area around the hole of the TEM foil. A Philips 400T electron microscope was used for the microstructure study.

3.3 Fractographic analysis

Fractured Single-edge-notched (SEN) specimens(7.6 mm thick by 25.4 mm wide by 132 mm long) used by Allision [1] in his corrosion fatigue crack growth study were examined. The specimens were in the TL (transverse-longitudinal) orientation, and were tested in four point bending under constant ΔK conditions (ΔK = 20 MPa$\sqrt{m}$ for the annealed material, and ΔK=20 and 30 MPa$\sqrt{m}$ for the cold-rolled material, with R=0.1) over a frequency range from 0.1 to 10 Hz. Fatigue tests in 0.6M NaCl aqueous solution were conducted under potentiostatic control at an externally applied potential, of -400 mV with respect to a saturated calomel reference electrode (SCE). The solution was prepared by dissolving sodium chloride (certified ACS) in deionized water, and was deaerated with high purity nitrogen to an oxygen concentration less than 0.01 ppm [1]. Fatigue crack growth tests in

air were performed only at 10 Hz. Wedged-opening-load(WOL) type specimens were used for tests in vacuum. Additional experimental information may be obtained from Allision's dissertation[1].

Fracture surface was first ultrasonically cleaned in acetone for 15 minutes, and then in methenol for 10 minutes, and finally in ethanol for 10 minutes and dried in air.

An ETEC Auto scan electron microscopy was used for fractographic analysis of the fatigue fracture surfaces. SEM was generally operated at 20 kV, with a working distance from 15 to 25 mm. The specimens were tilted from 0 to 15 degree about an axis parallel to the direction of crack growth.

3.4 Crystallographic and quantitative analysis of fracture facets

An etching pit method was chosen to identify the orientation of fine fracture facets, because the facets were too small (<300 μm) for X-ray diffraction analysis.

For cubic materials, suitable reagent can preferentially attack specific crystallographic planes. The resulting shape of an etch pit will be a polyhedral, formed by the intersection of the crystal with the etch pit faces, and will reflect the crystallographic orientation of the etched surface. Meletis et al. showed the geometric etch pit shapes for the three principal planes and the corresponding shape of etch pit surfaces, associated with preferential attack of {001} palnes in [11]. By examing the geometric shapes of the etch pits by SEM and by measuring the angles between the traces of intersecting etch pit faces, the orientation of the crystal surface can be determined [7].

For this AISI 304 stainless steel, one series of standard etching pits were prepared for comparison with the etching pits in the fracture facets. An annealed specimen was prepared to produce a very flat, polished surface. The etching pits were formed by electroetching in 10% oxalic aqueous solution, at 6 volts and room temperature.

The fracture surface was then etched under identical condition to produce etching pits on the fracture facets. SEM was used to investigate the etching pit geometry and to identify the crystallographic orientation. Specimen tilting was not

used in the SEM so as to maintain the geometrical identity(i.e., avoid the effects of foreshortening).

For quantitative analysis of facets, the Micro-Plan II digital analyzer was used to measure the areal fraction of facets over the entire fracture surface.

3.5 Cross-section studies

In order to resolve the microstructure beneath the fracture facets, a cross-section method was used. A transverse section was made through the fracture surface by carefully cutting with a diamond blade, with adequate cooling fluids, to minimize mechanical deformation and avoid overheating. The cut surface was then ground and polished until it intersected a fracture facet. The fracture surface was protected from damage during grinding and polishing the cross-section of specimen, and much attention was paid to keep the edge of cross section sharp. After polishing, electroetching was used to reveal the microstructure.

3.6 Crack path studies

In order to investigate the fatigue crack growth path in annealed 304 stainless steel, a compact tension(CT) specimen was cyclically loaded in air at a low stress intensity level to introduce a fatigue crack. Before fatigue testing, the specimen was ground, polished and lightly etched in 10% oxalic aqueous solution, operated at 6 volts and room temperature to reveal the microstructure. After fatigue testing, the crack path through the microstructure was examined by using polarized light illumination to enhance color contrast.

3.7 X-ray diffraction analysis

X-ray diffraction was used to determine the extent of martensitic transformation. Although the depth of x-ray penetration is large, 95 percent of the diffraction information refers to a depth of only about 25 μm, and 50 percent of that information originates in the first 5 μm [28]. Therefore, the x-ray diffraction analysis is well suited for investigating martensitic transformation in the thin layer near the fracture surface. In this study, an APD1700 Automated Powder Diffractometer

System I was used to provide quantitative estimates of the amount of alpha prime martensite.

Quantitative x-ray diffraction analysis is based upon the principle that the integrated intensity of the diffraction pattern of a specified phase depends on the volume fraction of that phase in the mixture. For quantitative analysis, the direct comparison method was used to estimate the relative amounts of austenite and martensite:

$$\frac{I\gamma}{I\alpha} = \frac{R\gamma}{R\alpha}\,\frac{C\gamma}{C\alpha}$$

where

I = integrated intensity,

$$R=\left(\frac{1}{V^2}\right)\left[\,|F|^2\,P\,\left(\frac{1+\cos^2\theta}{\sin^2\theta\,\cos\theta}\right)\,\right](e^{-2m})\,,$$

V= volume of unit cell,

F= structure factor,

P= multiplication factor, and

C= phase volume fraction.

In this study, austenite {111} peak and martensite {110} peak were chosen for the quantitative analyses. The lattice parameters and crystal structures of both austenitic and martensitic phases were determined for use in the R calculations. The crystal structure of austenite is face-center cubic, with lattice parameter a= 0.358 nm. The crystal structure of martensite is body-center cubic, with lattice parameter a= 0.287 nm.

Chapter 4 : EXPERIMENTAL RESULTS

4.1 Microstructure

The microstructures of the annealed and cold-rolled AISI 304 stainless steels were studied by both optical microscopy and conventional transmission electron microscopy. Figure 1(a) shows optical typical microstructure of an annealed 304 stainless steel with equiaxed grains and annealing twins, some of the twins appear to pass through half of the grain in this cross-section. The grain size of annealed material was about 60 μm based on the optical microstructure measurement. The difference in color reflect differences in crystal orientation. Figure 1(b) shows the typical TEM microstructure of annealed 304 stainless steel with annealing twins and dislocations.

Figure 2(a) shows optical microstructure of the cold-rolled material, with deformed grains, twins and slip bands. Figure 2(b) shows TEM microstructure of the cold-rolled material, with microtwins and stacking faults.

Both the annealed and cold-rolled materials were austenitic; no epsilon phase was detected by x-ray diffraction. The cold-rolled material contains a large amount of lattice defects, such as microtwins and stacking faults. These defects provide a high potential for martensitic transformation. The stacking faults has the same atomic packing sequence as epsilon martensite, which is ABABAB... . In contrast, the annealed material has a relatively low potential for martensitic transformation, because the microstructure consists of well-anneal grains and annealing twins.

4.2 Fracture surface morphology

4.2.1 The fracture surface morphology of annealed AISI 304 stainless steel

The fracture surface morphologies were studied. Fracture surfaces were produced by fatigue crack growth in 0.6M NaCl solution, air and vacuum at ΔK=20 MPa$\sqrt{m}$, R=0.1 and frequency ranging from 0.1 to 10 Hz. Typical fracture surface morphology in the aqueous solution consisted mainly of the following four components: (1) light-reflective flat facets over the fracture surface, see Figure 3; (2) a very small amount of well defined intergranular separation, Figure 4;

(3) microcracks out of the macroscopic plane of fracture, namely secondary cracks, Figure 3; and (4) the regions between the facets, which are characterized by features that are commonly termed quasi-cleavage, Figure 3(for more detail see Figure 5). The fracture surface morphology of annealed material in air and in vacuum are shown in Figs. 6 and 7, respectively. The fracture surface morphology in 0.6M NaCl and air are essentially the same and are brittle in nature. The fracture surface morphology in vacuum was ductile in nature and did not contain light-reflective facets. The morphology was totally different from that in aqueous solution and air. These observations shows that the environment did interact with the microstructure to produce different fracture surface morphologies under the same mechanical condition.

It is worth noting that quasi-cleavage was the predominant mode of fracture in the aqueous solution and air. However, the light-reflective fracture facets were well defined and were selected for further analysis.

4.2.1.1 Fracture facet analysis

Fracture facets were observed over the fracture surfaces which were produced in the aqueous solution and in air. Detailed features of the facet may be summarized as follows:

(1) Some facets are relatively featureless and others have fine structure, such as parallel steps, see Figure 6 for air, and Figs. 8, and 9 for aqueous solution. Figure 10 shows facets formed on parallel planes.

(2) The fracture surfaces appear to be matched one-to-one even at high magnification, Figs. 6, 8 and 9. Figures 6 and 9 show matching of facets and particle-hole and hole-hole pairs across mating fracture surfaces. The reason for a hole-hole pair is that the particle which was originally there had fallen out or was dissolved in the solution during corrosion fatigue.

(3) The facet sizes varied from about 10 to 50 μm, which are comparable to the austenite grain size. If the facet corresponds to the twin boundary (see detail later), then the facet sizes are compatible with the size of twins in the microstructure as shown in Figure 1(a).

(4) There were slip traces on some of the facets, Figure 11. The crystallographic directions of these traces will be determined from the etch pit analysis.

The areal fractions of facets over the fracture surfaces were measured. The amount of facets are shown as a function of 1/frequency in Fig. 12. The effect of frequency was not large. The percentages of facets are relatively small; being about 8.1±4.1 percent and 5.3±0.4 percent (estimated at 95% confidence) for annealed 304 stainless steel tested in the aqueous solution and in air at 10 Hz, respectively.

To further understand the role of facets in corrosion fatigue, the crystallographic orientation of the facets was determined by the etch-pit method. By comparison with the standard etching pits in Figure 13, the etching pit geometry which indicated that the facet plane corresponds to {111} in austenite. In FCC material, slip traces will form on {111} slip planes and along <110> directions. Figure 11(c) showed that the slip traces were parelled to one edge of the etching pit. This observation further confirmed that the facet plane was {111} type crystallographic plane.

4.2.1.2 Quasi-cleavage analysis

The regions between the facets represent the predominant mode produced by fatigue in the aqueous solution and in air. The morphology was more irregular, and quasi-cleavage in character, Figs. 3, 5 and 14. Etching pit method was applied to investigate the crystallographic nature of the quasi-cleavage region. Some of the quasi-cleavage regions showed well defined etching pits, Figure 14, and corresponded to cracking along $\{100\}_\gamma$ planes, as indicated by deep etching. So, the quasi-cleavage cracking were along macrocrystallographic planes (say {100} type plane).

4.2.1.3 Fracture surface morphology in vacuum

The fracture surface morphology in vacuum is totally different from that in aqueous solution and in air. There were no light-reflective fracture facets, no quasi-cleavage region, no grain boundary separation in the fracture surface in vacuum. Ductile deformation markings and relatively flat coarse striation-like regions form the major components of the fracture surface morphology in vacuum, Figs. 7

and 15.

4.2.2 The fracture surface morphology of cold-rolled AISI 304 stainless steel

The fracture surface produced by corrosion fatigue crack growth of cold-rolled 304 stainless steel in 0.6M NaCl solution were examined by scanning electron microscopy. The major morphology components are as follows: (1) very small amount of light-reflective facets, but smaller in size than those in annealed steel, Figure 16; (2) quasi-cleavage regions (surrounding the facets), Figure 16; and (3) secondary cracks, Figure 16 (at lower magnification). There was no well defined grain boundry cracking. The fracture surface in Figure 17 showed parallel laths, that are brittle in nature. According to the slip trace analysis, the facets corresponded to {111} type planes. Similar to the annealed material, the cold-rolled material showed closely matched mating region, with clearly defined particle-hole pair, Figure 18. Fracture surface morphology of cold-rolled material was also very sensitive to environment, Figure 19; with the morphology changed at the air and vacuum boundary. The fracture surface morphology produced in vacuum was ductile in nature, Figure 20 , and showed slip markings, Figure 21.

4.3 Crack path and microstructure

In order to understand the role of microstructure in corrosion fatigue crack growth, a metallographic cross-section method was used to examine the microstructure in relation to specific components of the fracture surface morphology; for example, the light-reflective facets produced in annealed 304 stainless steel in air and in the aqueous solution. A typical example is shown in Fig. 22, where a twin boundary is identified with a flat fracture facet.

To further examine the crack path, the same method was used on a fatigue sample tested in air. The fatigue crack path and the underlying microstructure are shown in optical micrographs taken with polarized light illumination to enhance contrast, Figs. 23–25. Cracking was predominantly transgrannular with respect to the austenite grains, Figure 23. Some cracking along a twin boundary and an austenite grain boundary may be seen in Figs. 24 and 25, respectively. Whether the fatigue crack went along a twin boundary or not depended upon its orientation with

respect to the main crack so as to maintain macroscopically Mode I cracking.

Based on the low magnification micrographs, the maximum angle of deviation of the twin boundary cracks, from the expected direction of crack growth was determined. Figure 26 showed the schematic diagram of crack path. This angle was found to be about 28 degrees based on the two dimensional measurement. For determining the true angle, additional sections are needed to take the third dimension into account.

The path of a fatigue crack in vacuum, relative to the microstructure, was examined, and no twin boundary and grain boundary separations were observed.

4.4 Martensite transformation near the fracture surface

To evaluate the role of fatigue induced transformation to alpha prime martensite on corrosion fatigue crack growth, quantitative x-ray diffraction analyses were performed on the fracture surfaces. The original annealed and cold-rolled stainless steels show γ austenitic phase, Figs. 27 and 28. The materials after fatigue testing in vacuum, air and 3.5% NaCl solution, show the α' martensitic transformation, Figs. 29-34. The results of martensitic transformation are given in Table III. In the annealed material, the amount of α' martensite in the material fatigue in vacuum was found to be much more than that in aqueous solution and in air. No distinct ϵ martensite was detected by x-ray diffraction on the fracture surface. In the cold-rolled material, the situation was different. The volume fractions of α' martensite in cold-rolled material are essential the same in all three environments. Again no distinct ϵ martensite was detected on the fracture surface by x-ray diffraction.

Chapter 5 : DISCUSSION

5.1 Facet analysis

The fracture surfaces of annealed 304 stainless steel tested in 0.6M NaCl solution and in air contained very flat, light-reflective facets. Although the amount of facets were small, these facets were well defined. To better understand the origin of these facets, the crystallographic orientation of the facets was determined by an etch pit method. The etching pits were triangular in shape, with one of the etching pit edges parallel to slip traces, Figure 11(c). Based on the etching pit geometry, the plane of the facets was identified as being of {111} type in the fcc material. The facet orientation was further confirmed by slip trace analysis. Because the $\{111\}_\gamma$ slip planes would intersect a $\{111\}_\gamma$ plane to form slip traces along <110> directions, the angle between two intersecting slip traces would be a 60 degrees . The analyses of etching pits and slip traces were based on the fcc type material.

Examinations of transverse sections showed that the facets are always associated with annealing twins, and represent cracking along the twin boundaries in austenite. Figures 23, 24 and 25 show cracking along some twin boundaries and grain boundaries, but mostly by transgranular cracking. Because twins are usually well separated, and the amount of twin boundary cracking (or number of facets) would be limited. Because of orientation considerations, the fracture surface would seldom show intersecting facets, but could have parallel facets, or facets with steps corresponding to the incoherent boundaries seen along twins in the microstructure[29]. The facet surface morphologies were different; some being simple and some having parallel steps(see Figures 3, 8, 9 and 10). This difference may be explained by the boundary microstructure, and further confirms that the facets represent twin boundaries.

The above discussion indicate that the facets and etching pits are associated with a fcc crystal structure. Liu et al. [3] reported that for a 304 type material tested in $MgCl_2$ at 289^o C, no martensitic phases were detected at the fracture surfaces and there were large and flat fracture facets. This means that the flat facets must be associated with the austenitic phase. Caskey [27], using wide-angle x-ray, showed the presence of austenitic, alpha prime and epsilon phases on fractured 304L

type material. However, Laue back-reflection patterns from characteristic brittle facets only gave patterns for austenite. All of the evidence show that the material adjacent to the fracture facets (twin boundary) remained austenitic.

5.2 Role of twin boundaries

The experimental results showed that deleterious test environments altered the fracture surface morphology from ductile transgranular cracking to brittle $\{111\}_\gamma$ twin boundary and quasi-cleavage separation. The preference for twin boundary separation depends on the orientation of the twin boundary with respect to the loading axis to maintain "in plane" Mode I crack growth. A schematic sketch of the crack paths in annealed AISI 304 stainless steel is given in Fig. 26.

The role of twin boundary and grain boundary in environmentally assisted fatigue crack growth was assessed by Gao et al. [30] using the following analysis: The total linear fraction of twin and grain boundaries, A can be expressed by:

$$A=\sum\{\Delta S_i \cos(\theta_i)\ F_i(\theta_i) / d_i\}$$

Where

ΔS_i : the maximum distance of crack growth along ith boundary (either twin or grain boundary),

θ_i : the angle between main crack and boundary,

d_i : the size of the corresponding grain, and

$F_i(\theta_i)$: the probability of occurrence of the events identical to ith boundary cracking.

For simplicity, the average crack growth distance Δl and average grain size d are taken.

$$A = \Delta l \quad (F / d)$$

This equation predicts that the linear fraction of twin-grain boundary cracking increases as the grain size decreases, and reaches its limit, A = F when d approaches Δl.

The role of twin boundary cracking in environmentally assisted fatigue crack growth can be estimated by a superposition model by assuming that the areal fraction of twin boundary separation on the fracture surface is equal to A.

$$(\frac{da}{dN})_e=(\frac{da}{dN})_{e,matrix}\ (1-A) + (\frac{da}{dN})_{e,g}\ A\ , \text{ then}$$

$$(\frac{da}{dN})_e = (\frac{da}{dN})_{e,matrix} + [(\frac{da}{dN})_{e,g} - (\frac{da}{dN})_{e,matrix}]\ A$$

Where

$(\frac{da}{dN})_e$: crack growth rate of the material in environment

$(\frac{da}{dN})_{e,matrix}$: crack growth rate through matrix ,

$(\frac{da}{dN})_{e,g}$: crack growth rate along twin or grain boundary.

From this equation, assuming $(\frac{da}{dN})_{e,g} > (\frac{da}{dN})_{e,matrix}$, if A increases, then $(\frac{da}{dN})_e$ will increase.

Therefore if grain size decreases, the crack growth rate in environments will increase. This implies that grain refinement may not be beneficial from the corrosion fatigue crack growth point of view. This prediction needs further experimental verification.

5.3 Martensitic transformation

The issue is whether martensitic transformation is required for hydrogen embrittlement of the metastable austenitic stainless steels. From the study of annealed material, the amounts of α' martensite near the fracture surface in 0.6M NaCl solution and in air were found to be much lower than that observed in vacuum (40% versus 80%). In the cold-rolled material, on the other hand, the amounts of α' martensite were nearly the same for all of the environments (80%)(see Table III). This implies that the α' martensite transformation was not enhanced by hydrogen, and transformation was not required for hydrogen embrittlement. The difference in the amount of α' martensite in annealed and cold-rolled stainless steels in 0.6M NaCl aqueous solution may be explained by microstructural differences. Murr et al. [31] reported that α' martensite nucleated only at shear band intersections. Shear bands consist of bundles of stacking faults, twins (or ϵ- martensite). The microstructure of cold-rolled material (see Figure 2) show the deformed grains, with microtwins and

slip bands. These defect sites have a high potential for martensitic nucleation, and require less strain to effect transformation.

In the absence of hydrogen (i.e. in vacuum), the amount of alpha prime martensite in the annealed and cold-rolled stainless steels was almost the same, at about 80 vol%; i.e. , at nearly the saturated amount according to Hecker[19]. Thus, crack-tip strain is primarily responsible for α' martensite transformation. The lower amount of transformation (~40 vol%), for the annealed material suggests embrittlement by hydrogen had severely limited the strain that could be attained.

The results suggest that the amount of transformation was determined by the maximum strain at the crack tip and by the initial microstructure.

Hanninen et al. [32] rerported that the fracture surface of hydrogen-charged AISI 316 type material did not showed any martensite. This suggested that the α' martensitic transformation is not required for hydrogen embrittlement. The lower amount of α' martensite in 0.6M NaCl solution and in air for the anneal material is in agreement with this interpretation. The relative susceptibility of martensite and austensite to environmental cracking, however, may be different. Schuster et al. [7] reported that the difference in fatigue crack growth rates of type 301 and 302 stainless steel in hydrogen was due to their difference in austensite stability(301 less stable than 302). Their arguments are as follows:

(a) hydrogen permeation through α' martensite is higher than γ austensite.

(b) α' martensite might crack more easily than the γ phase.

From this study, the cold-rolled material showed higher fatigue crack growth rate than the annealed material in 0.6M NaCl solution(see Figure 35), while the cold-rolled material also had more α' martensite on fracture surface. In essence, α' martensite does seem to be more susceptible to environmental cracking than the austensite. However, the next question to consider is whether the α' martensite is fully responsible for the observed difference in fatigue crack growth rate between the annealed and cold-rolled materials.

5.4 Role of martensitic transformation in corrosion fatigue

Figure 27 shows a comparison between the fatigue crack growth rates of annealed and cold-rolled materials tested at $\Delta K=20$ MPa$\sqrt{m}$ and 298K in 0.6M NaCl solution(at pH=6.5 and -400 mV SCE) [1]. The fatigue crack growth rates in the cold-rolled material are seen to be 3~4 times higher than those in the annealed material. Before fatigue testing, the microstructures of two materials are different, and after testing, the amount of α' martensite on the fracture surface are also different.

The contribution of α' martensite to the fatigue crack growth rate may be estimated by the superposition model[32].

$$(\frac{da}{dN})_e = (\frac{da}{dN})_r(1- \Phi)+ (\frac{da}{dN})_c \Phi$$

where

$(\frac{da}{dN})_r$ = mechanical fatigue rate,

$(\frac{da}{dN})_c$ = " pure " corrosion fatigue rate, and

Φ = fractional area of crack that is undergoing pure corrosion fatigue.

For more than one cracking element, the superposition model may be rewritten as following :

$$(\frac{da}{dN})_e = \sum[(\frac{da}{dN})_{ei} f_i]$$

where

$$(\frac{da}{dN})_{ei} = (\frac{da}{dN})_{ri}(1- \Phi_i) + (\frac{da}{dN})_{ci} \Phi_i$$

i : ith cracking element,

f_i : areal fraction of ith element, and

Φ_i : areal fraction of ith element undergoing pure corrosion fatigue.

In the present study, two elements are considered; one is the austenitic phase(A) and the other, the martensitic phase(M). Therefore,

$$(\frac{da}{dN})_e = (\frac{da}{dN})_{e,A} f_A + (\frac{da}{dN})_{e,M} (1- f_A)$$

$$(\frac{da}{dN})_{e,A} = (\frac{da}{dN})_{rA}(1- \Phi_A) + (\frac{da}{dN})_{cA} \Phi_A$$

$$(\frac{da}{dN})_{e,M} = (\frac{da}{dN})_{rM}(1-\Phi_M) + (\frac{da}{dN})_{cM}\Phi_M$$

To further simplify the estimation, only the crack growth rate in 0.6M NaCl solution at the saturation level (or for pure corrosion fatigue) is considered, i.e., $\Phi_A = \Phi_M = 1$. As such,

$$(\frac{da}{dN})_{e,A} = (\frac{da}{dN})_{cA} \ , \quad (\frac{da}{dN})_{e,M} = (\frac{da}{dN})_{cM}$$

$$(\frac{da}{dN})_e = (\frac{da}{dN})_{cA} \ f_A + (\frac{da}{dN})_{cM} \ (1-f_A)$$

For this estimate, crack growth rate in α' martensite is assumed to be 10 times higher than in the austenite, i.e., $(\frac{da}{dN})_{cM} = 10 \ (\frac{da}{dN})_{cA}$, and therefore,

$$(\frac{da}{dN})_e = (\frac{da}{dN})_{cA} \ [10-9 \ f_A]$$

The areal fraction f_A is taken to be equal to the volume fraction of austenitic phase determined from the x-ray measurements(see Table III); for the annealed material, $f_A = 0.6$ and for the cold-rolled material $f_A = 0.3$ at $\Delta K=20$ MPa$\sqrt{m}$ in 0.6M NaCl solution. Using these values, fatigue crack growth rate enhancement by α' martensite is estimated to be only a factor of 1.6, and cannot account for the observed difference in fatigue crack growth rate between the annealed and cold-rolled materials. This suggests the α' martensite transformation played only a secondary role in the corrosion fatigue of 304 stainless steels.

Other reasons for the difference in fatigue crack growth rate need to be considered. One such reason may be the basic difference in microstructure , such as microtwins, dislocation densities, and stacking faults. The cold-rolled material has a high density of microtwins(Figure 2(b)). The microtwins are about 15 nm in thickness, and the twin boundaries are the preferred cracking paths. These microtwins, therefore may be responsible for the difference in fatigue crack growth rate between the cold-rolled and solution-annealed materials.

In summary, the microstructure difference between the cold-rolled and annealed stainless steels is the main reason for the difference in crack growth rate between them.

Chapter 6 : SUMMARY

The roles of twin boundary and martensitic transformation in corrosion fatigue crack growth of solution-annealed and cold-rolled AISI 304 stainless steels were studied by metallographic, fractographic, crystallographic and x-ray diffraction techniques. A model proposed by Gao et al. incorporating the contributions by the twin boundary and α' martensite, was used to estimate the crack growth rate.

Fracture surface morphologies of annealed and cold-rolled AISI 304 stainless steels tested in 0.6M NaCl aqueous solution and in air were brittle, exhibiting shiny facets and quasi-cleavage features. The facets corresponded to $\{111\}_\gamma$ planes and were formed by cracking along the twin boundary. Fatigue cracking occurred primarily by $\{001\}_\gamma$, and other unidentified, quasi-cleavage. However, preferential cracking along the $\{111\}_\gamma$ twin boundaries and austenite grain boundaries occurred whenever these boundaries were favorably oriented with respect to the loading axis. Fatigue cracking in vacuum was ductile and non-crystallogrphic in nature.

Transformation to alpha prime martensite by fatigue was found to be essentially complete in cold-rolled steel, and in annealed steel, tested in vacuum, but was substantially less in the annealed steel, tested in air and 0.6M NaCl solution.

Based on x-ray analysis, metastable austenite to martensite transformation is not a prerequisite for hydrogen embrittlement of AISI 304 stainless steels. The contribution of martensite to fatigue crack growth rate was estimated and was judged to be of secondary importance. The difference in crack growth rates between the cold-rolled and annealed materials was attributed mainly to microstructural difference, such as microtwins, dislocations, stacking faults, etc..

These results, taken in conjunction with crack growth and electrochemical reaction data, support hydrogen embrittlement as the mechanism for corrosion fatigue crack growth in 304 stainless steels. Martensitic transformation is not necessary for hydrogen embrittlement and incidental to corrosion fatigue crack growth in these steels.

Table I : Composition of AISI 304 Stainless Steel

Condition	Chemical composition (Wt.%)							
	C	Cr	Ni	Mn	Si	Mo	P	S
Annealed(1)	0.054	18.53	9.75	1.22	0.48	0.32	0.03	0.02
Cold-rolled(2) (25%)	0.061	18.23	8.05	1.94	0.55	0.21	0.03	0.02

(1) Oak Ridge National Laboratory, Heat No. 922796

(2) Allegheny Ludlum Steel Corp., Heat No. 899586-63

Table II : Room Temperature Tensile Properties For AISI 304 Stainless Steels(1)

Condition	0.2% Offset Yield Strength (MPa)	Tensile Strength (MPa)	Elongation (%)	R.A. (%)
Annealed	208	594	80.2(2)	65.6
Cold-rolled (25%)	796	863	23.6(3)	N/A

(1) Average of three specimens

(2) Gage length=50.8 mm

(3) Gage length=12.7 mm

Table III Volume Percentage of Alpha Prime Martensite Near The Fatigue Fracture Surface at Room Temperature

Material and Test Condition	Environmental Condition		
	3.5% NaCl	Lab. Air	Vacuum
Annealed			
$\Delta K=20$ MPa$\sqrt{m}$	40	40	86 (1)
Cold-rolled			
$\Delta K=20$ MPa$\sqrt{m}$	70	N/A	80
$\Delta K=30$ MPa$\sqrt{m}$	83	73	83

(1) $\Delta K=24$ MPa$\sqrt{m}$

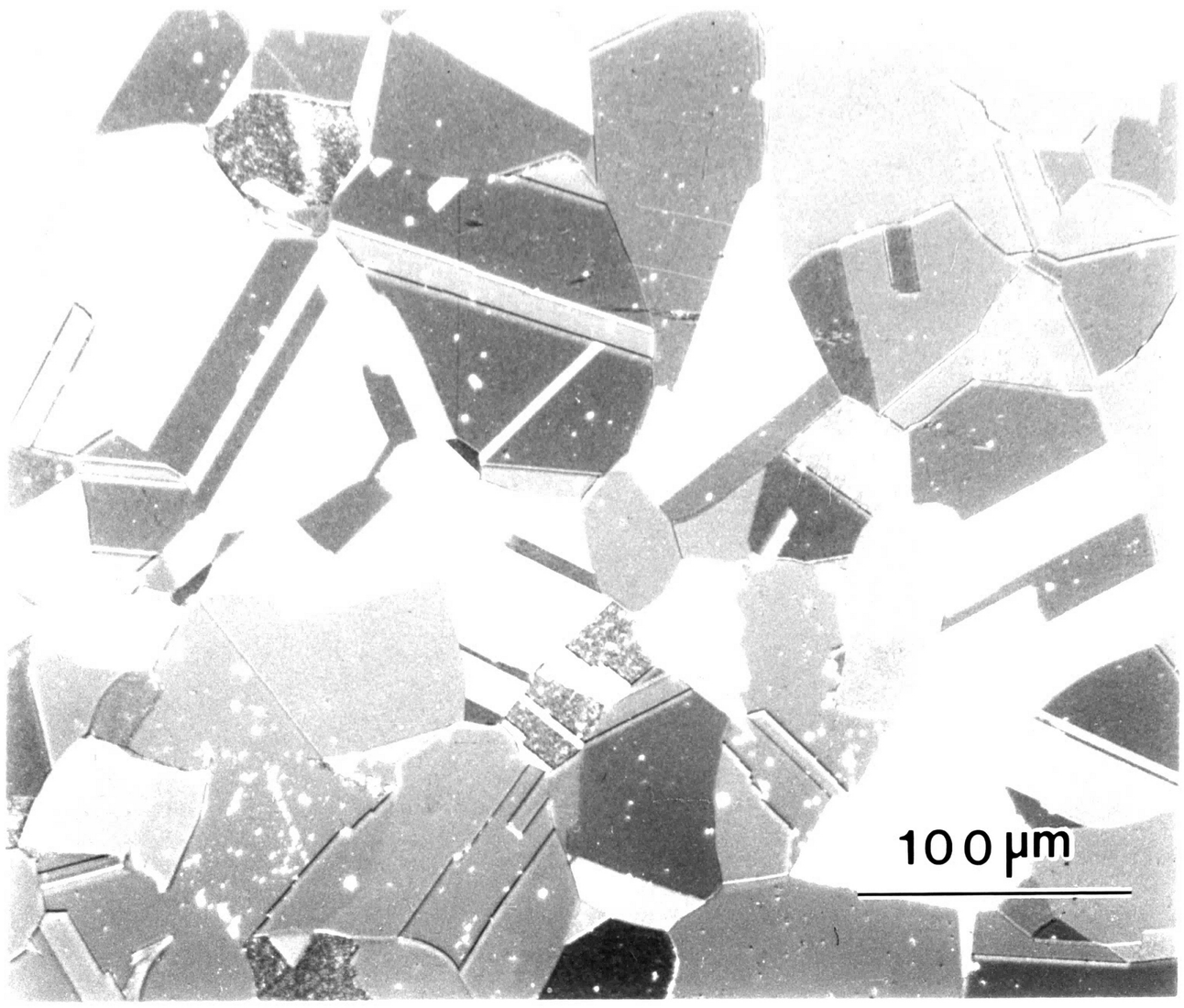

(a)

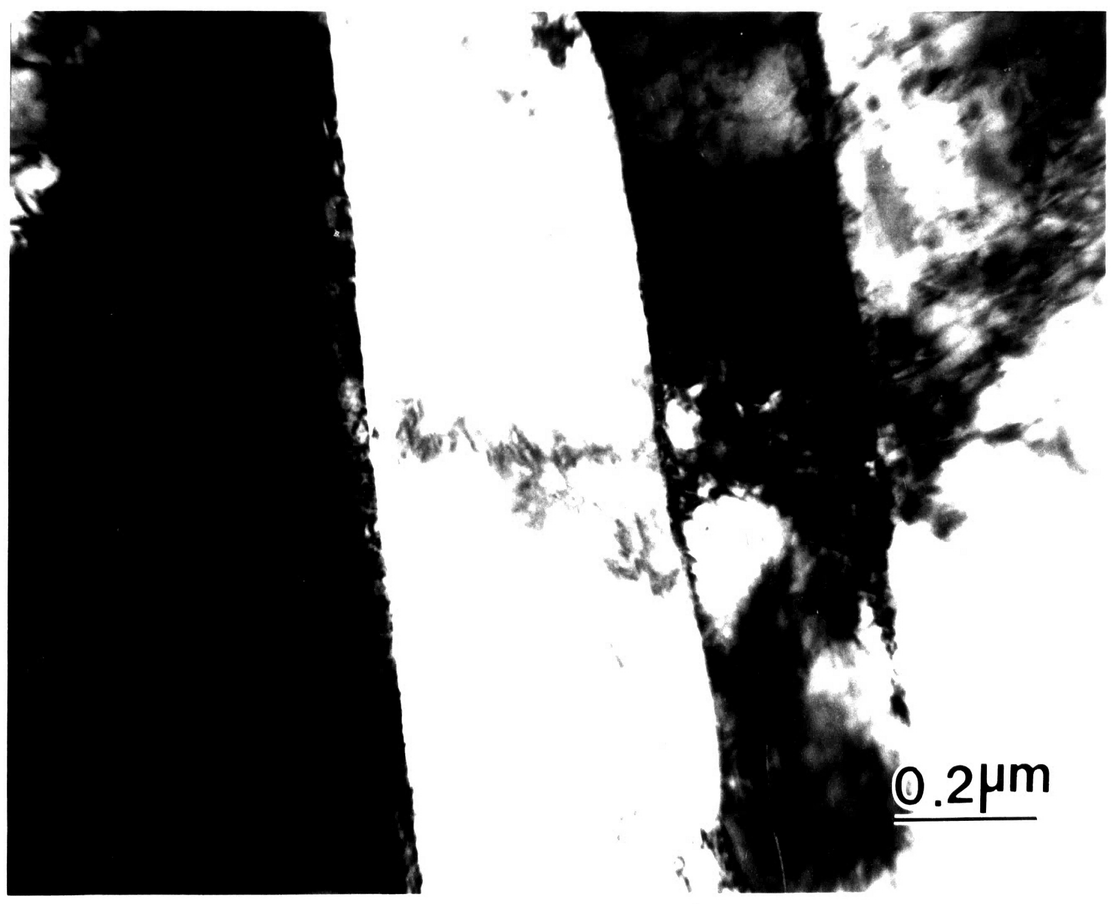

(b)

Fig. 1 Optical and TEM micrographs of annealed AISI 304 stainless steel showing (a) equiaxed grains and annealing twins, and (b) annealing twins and dislocations.

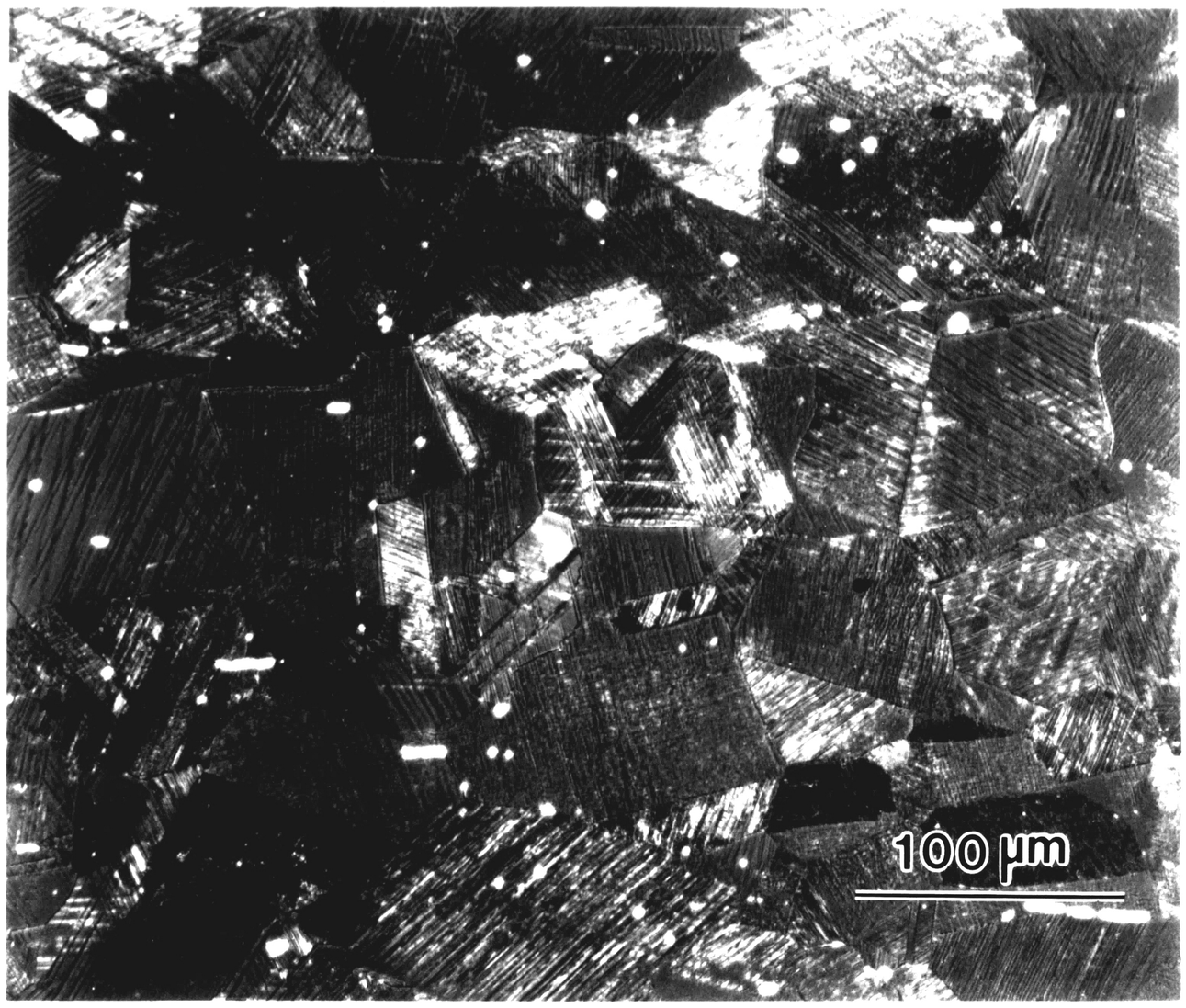

(a)

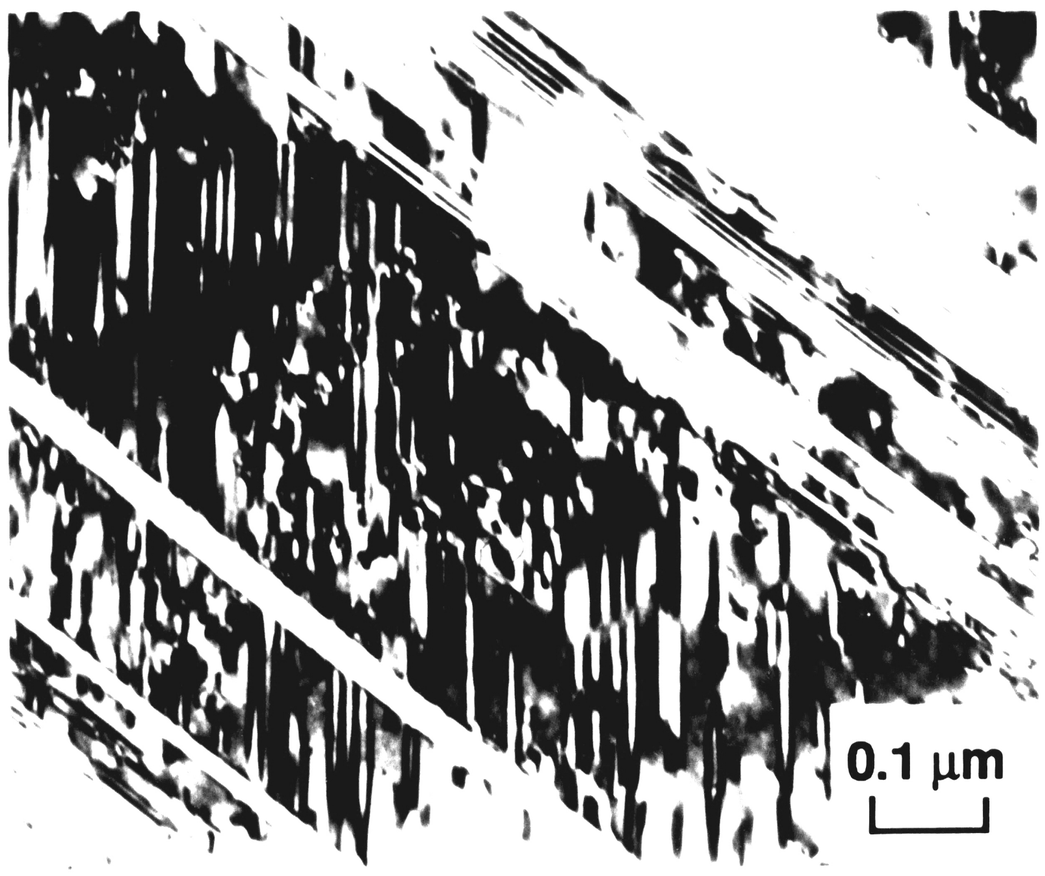

(b)

Fig. 2 Optical and TEM micrographs of cold-rolled 304 stainless steel showing (a) deformed grains, twins and slip bands, and (b) microtwins and stacking faults.

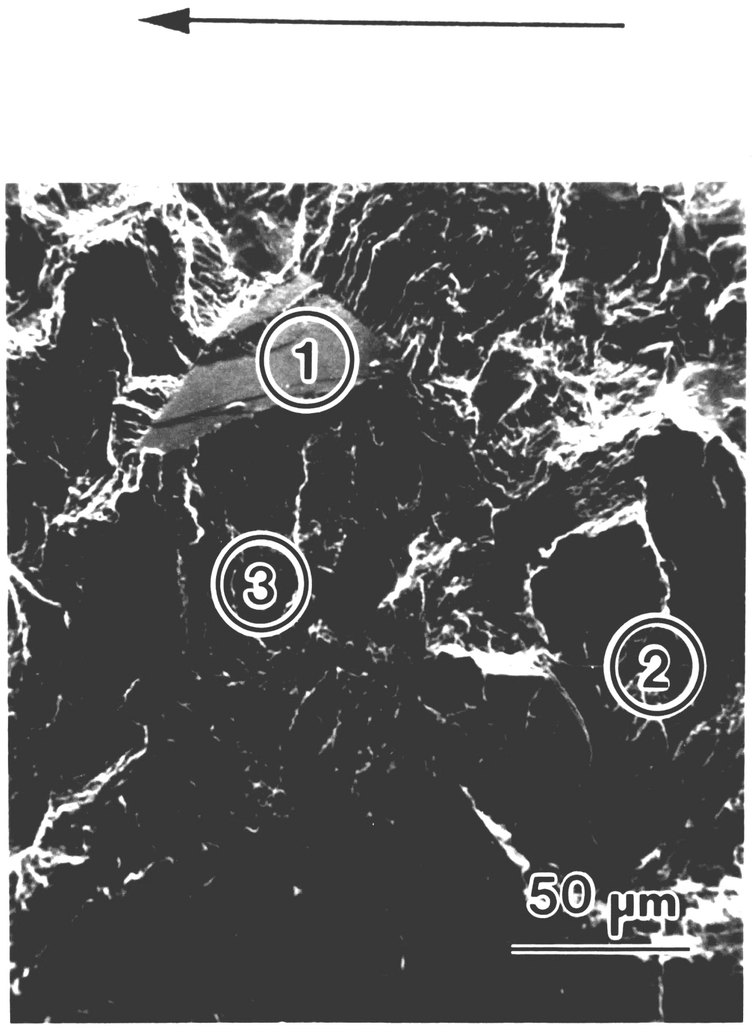

Fig. 3 SEM microfractograph of annealed 304 stainless steel tested in 3.5% NaCl solution at ΔK=20 MPa$\sqrt{m}$, R=0.1 and f=10Hz, 298 K showing (1) a flat facet (2) a secondary crack (3) irregular appearing regions.

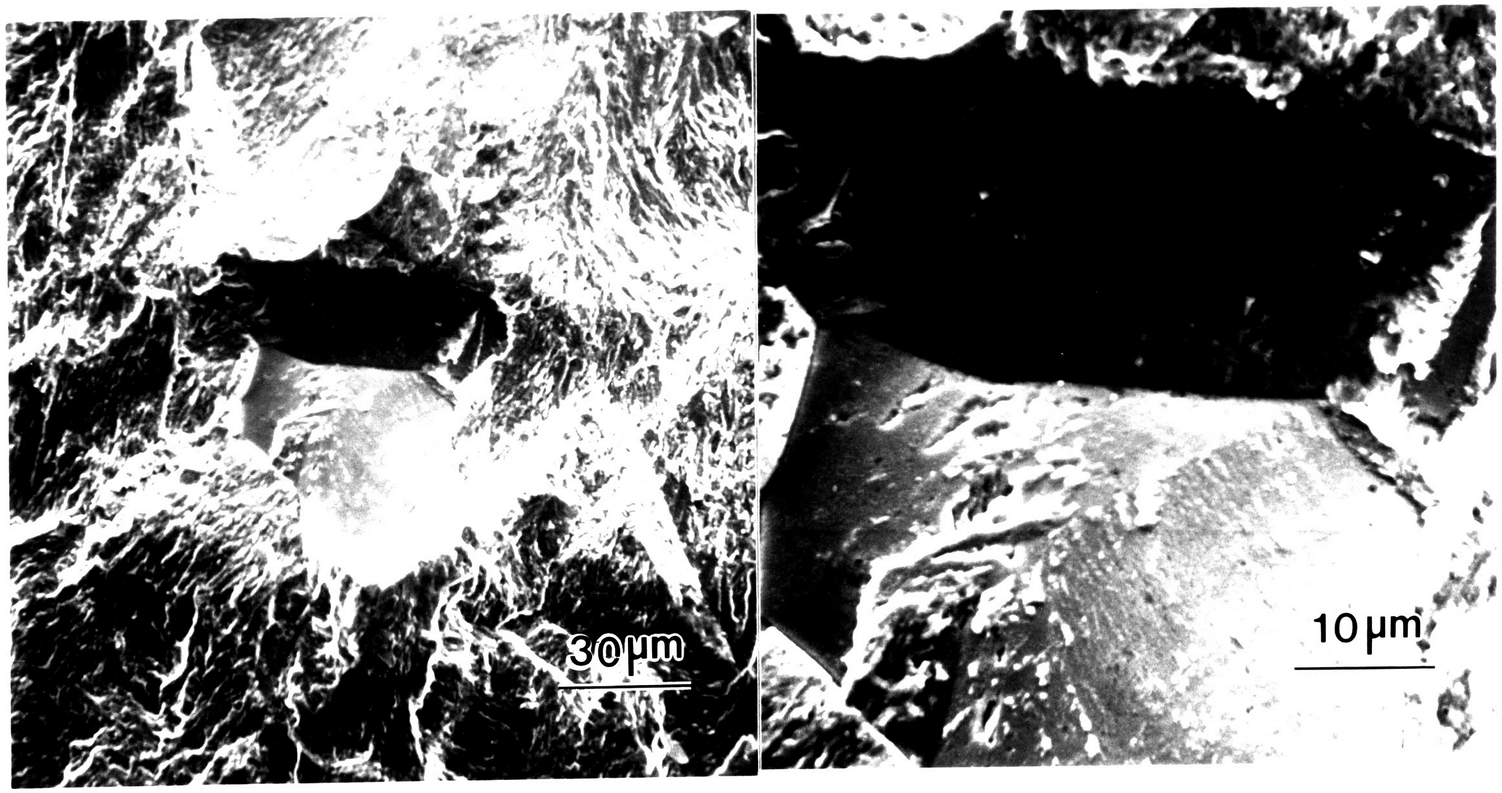

(a) (b)

Fig. 4 SEM microfrctographs of annealed 304 stainless steel tested in 3.5% NaCl solution at ΔK=20 MPa$\sqrt{m}$, R=0.1 and f=0.1 Hz, 298 K, showing cracking along austenitic grain boundaries at (a) low magnification and (b) high magnification.

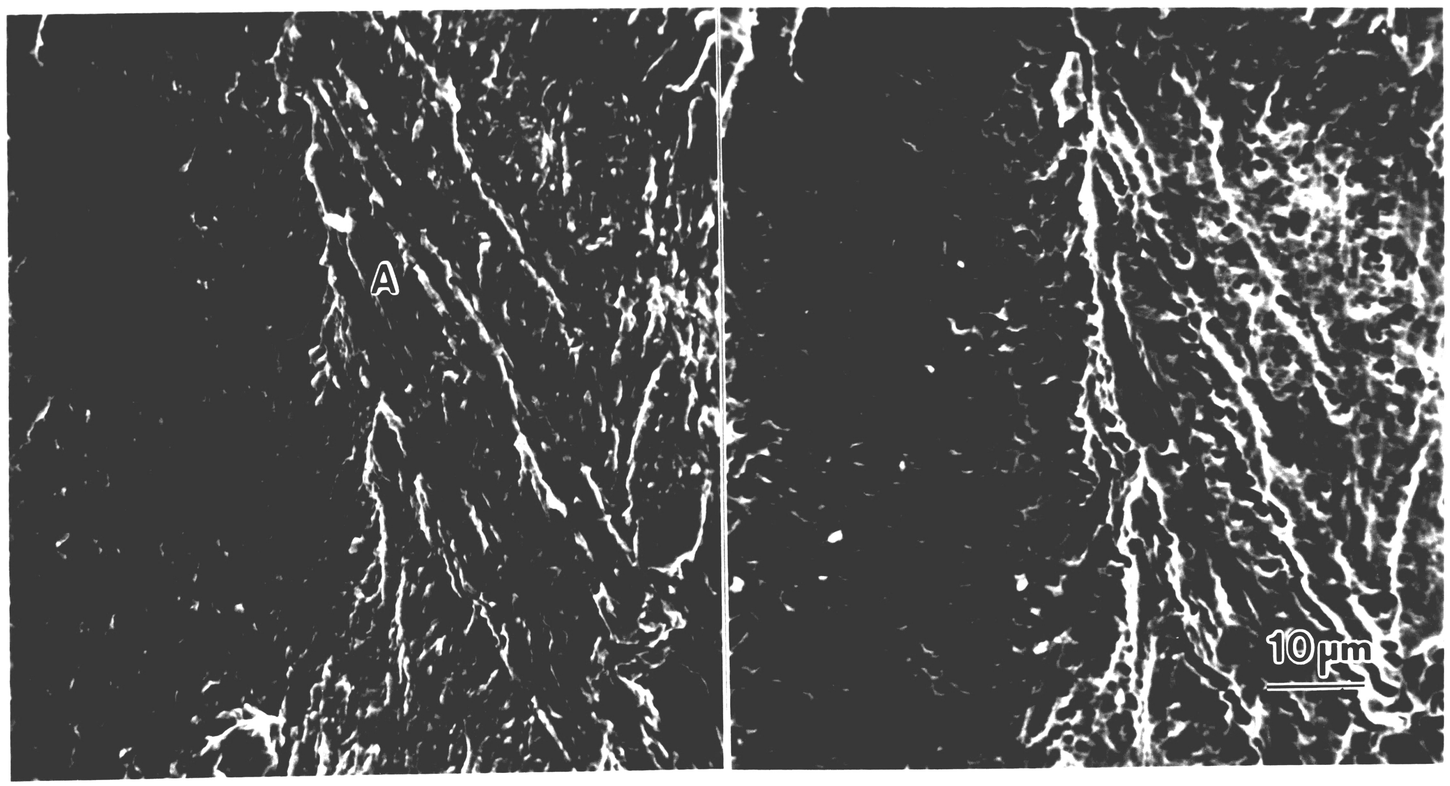

(a) (b)

Fig. 5 SEM microfractographs of annealed 304 stainless steel tested in 3.5% NaCl solution at ΔK=20 MPa$\sqrt{m}$, R=0.1 and f=10 Hz, 298 K, showing a quasi-cleavage (QC) region at high magnification: (a) before etching and (b) after etching. Note that the platelet-like features marked by A in (a) may be related to α' martensite, and that the etch-pits in (b) indicate the QC occurred along $\{001\}_\gamma$.

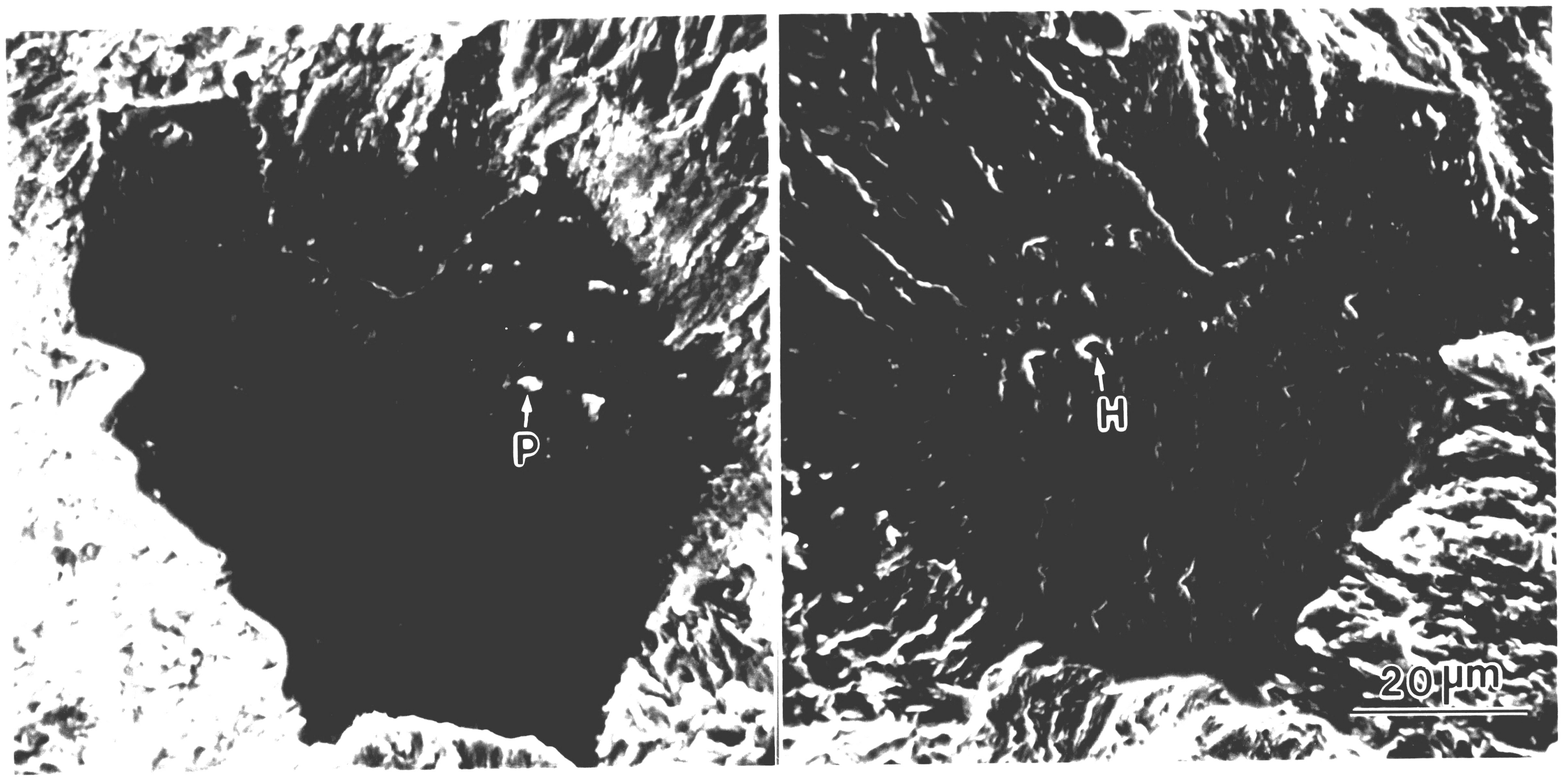

Fig. 6 SEM microfractographs of annealed 304 stainless steel tested in air at $\Delta K=20$ MPa$\sqrt{m}$, R=0.1 and f=10 Hz, 298K, showing the mating surfaces of a facet similar to that observed in 3.5% NaCl solution. Note: the particle-hole pair as indicated by P and H.

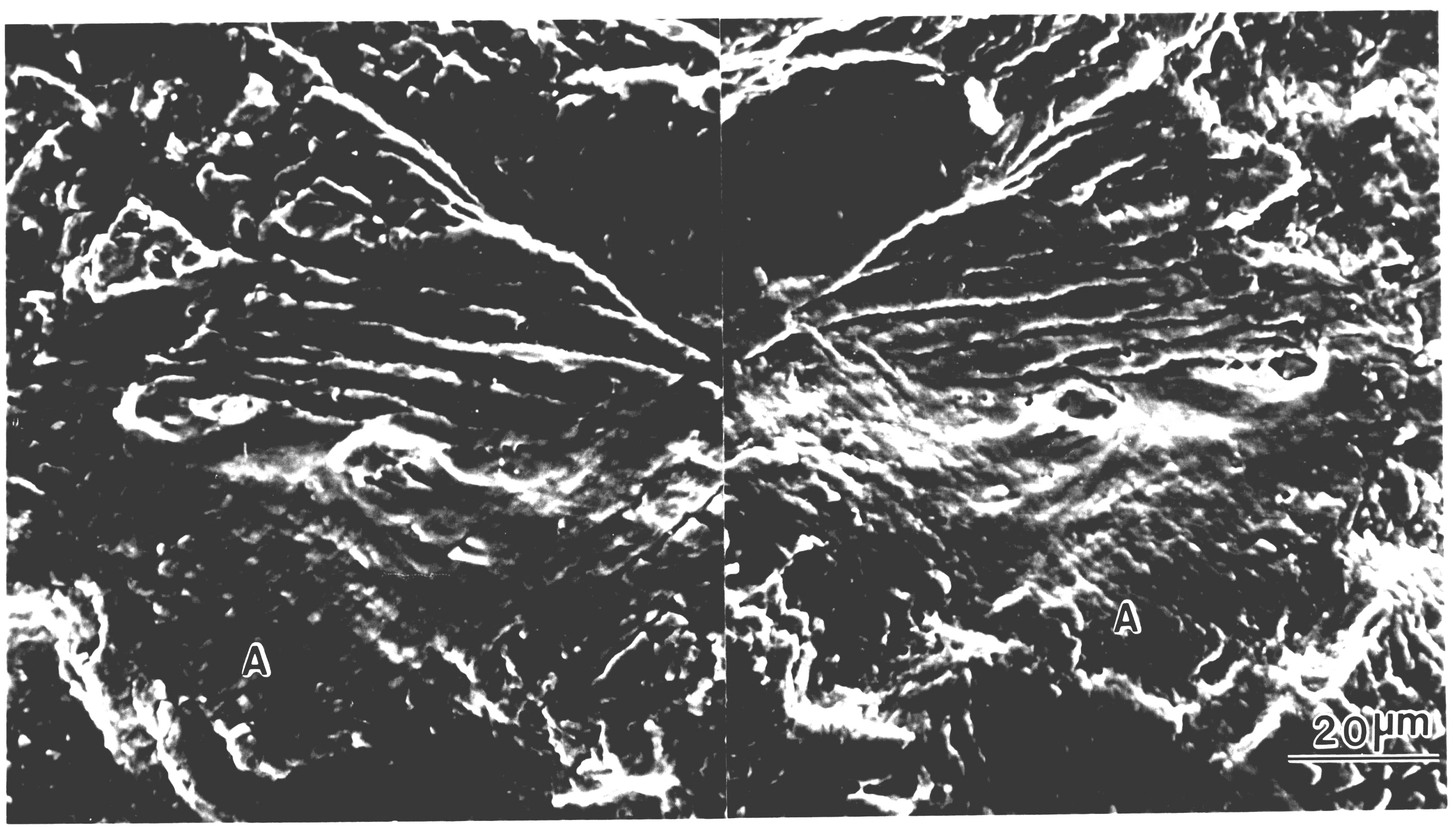

Fig. 7 SEM microfractographs of annealed 304 stainless steel tested in vacuum at 1.7×10^{-5} Pa at $\Delta K=24$ MPa$\sqrt{m}$, R=0.1 and f=8 Hz, 298 K, showing typical ductile striation-like markings.

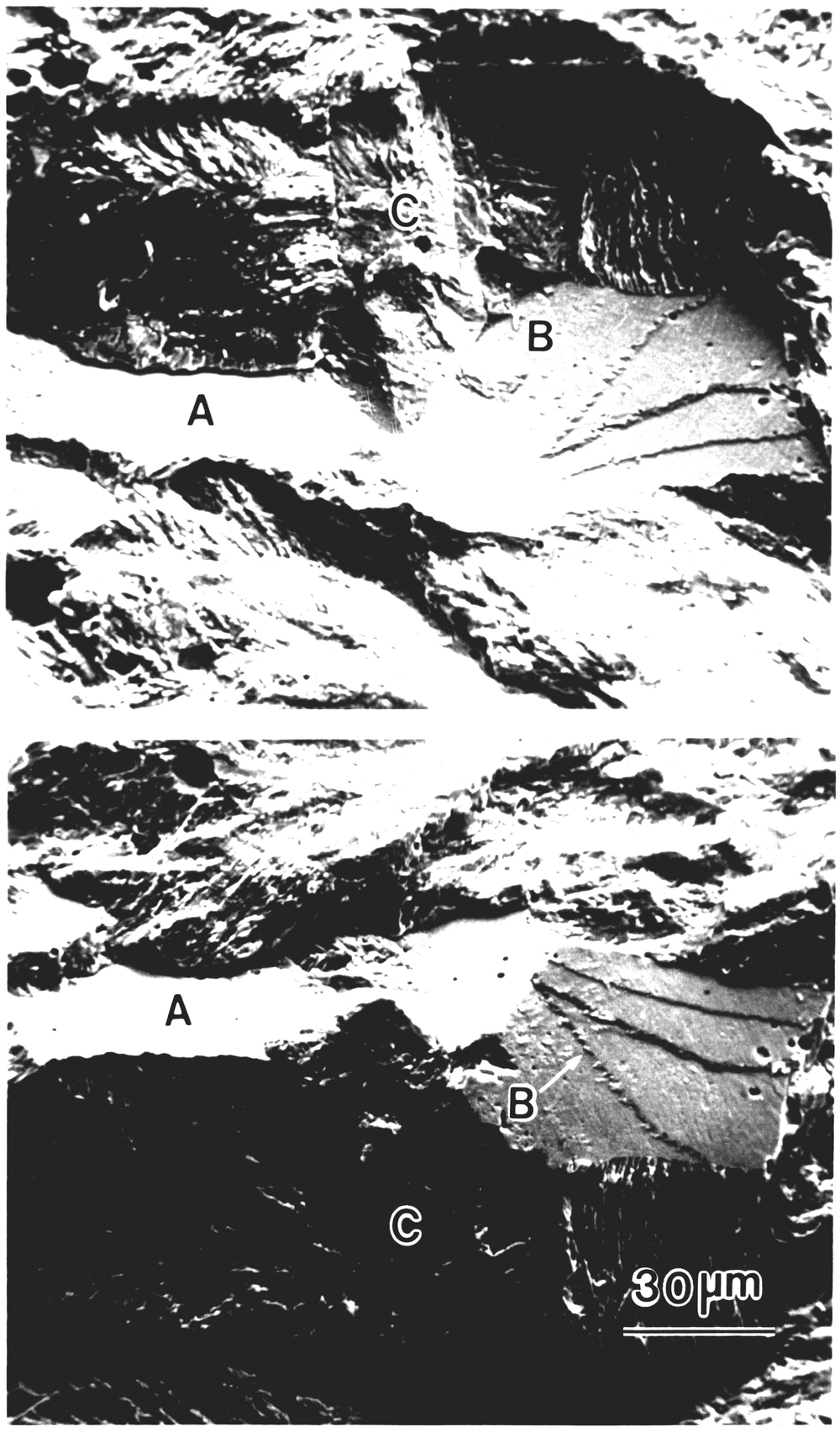

Fig. 8 SEM microfractographs from mating fracture surfaces of annealed 304 stainless steel tested in 3.5% NaCl solution at ΔK=20 MPa$\sqrt{m}$, R=0.1 and f=0.1 Hz, showing A-A: featureless flat facet; B-B: facet with steps; and C-C: irregular appearing regions between facets.

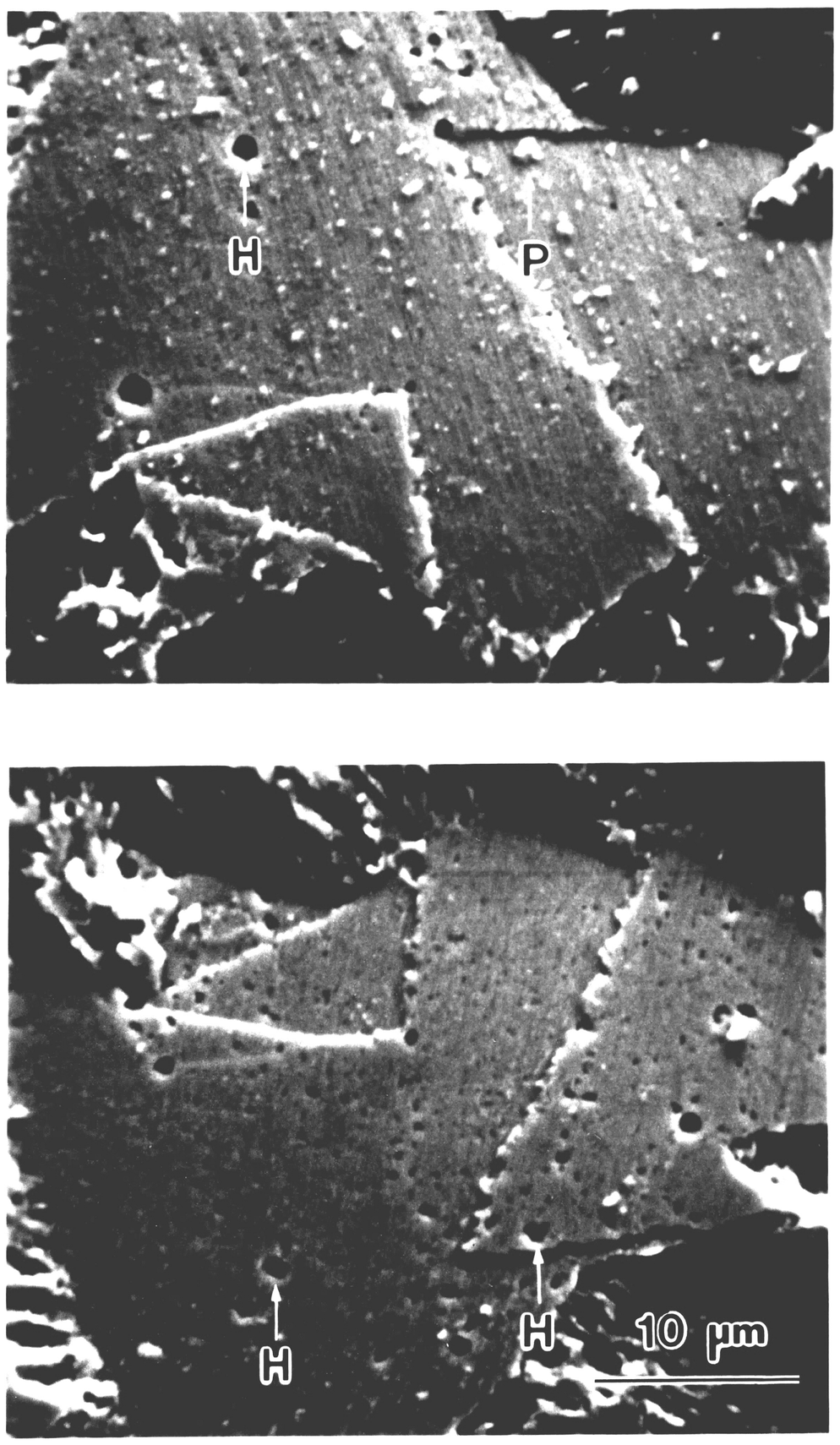

Fig. 9 SEM microfractographs from mating fracture surfaces of annealed 304 stainless steel tested in 3.5 % NaCl solution at ΔK=20 MPa$\sqrt{m}$, R=0.1 and f=0.1 Hz, 298 K, showing particle-hole pair (P-H) and hole-hole pair (H-H).

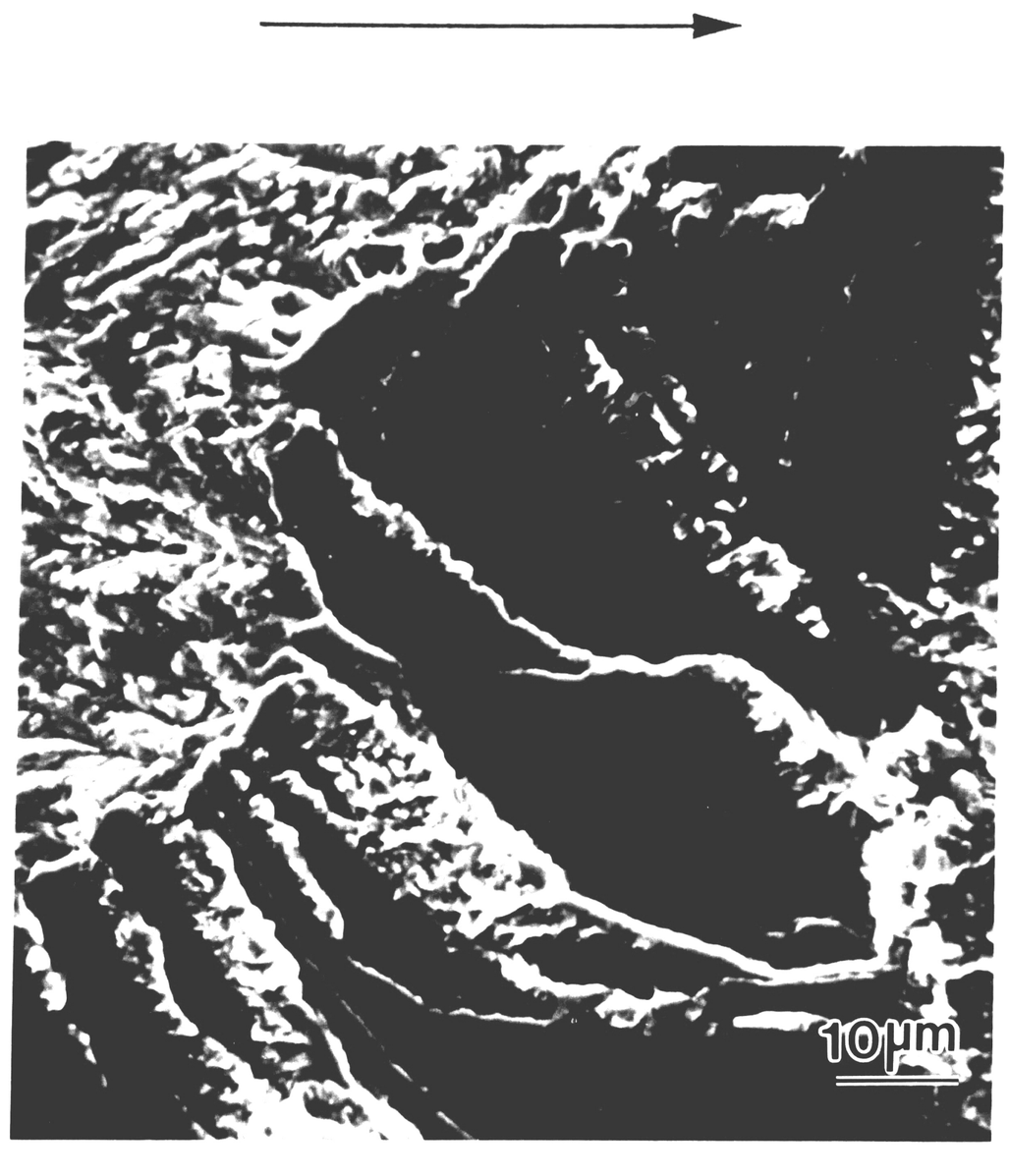

Fig. 10 SEM microfractographs of annealed 304 stainless steel tested in 3.5% NaCl solution at ΔK=20 MPa$\sqrt{m}$, R=0.1, and f=5 Hz, 298 K, showing a series of facets in steps.

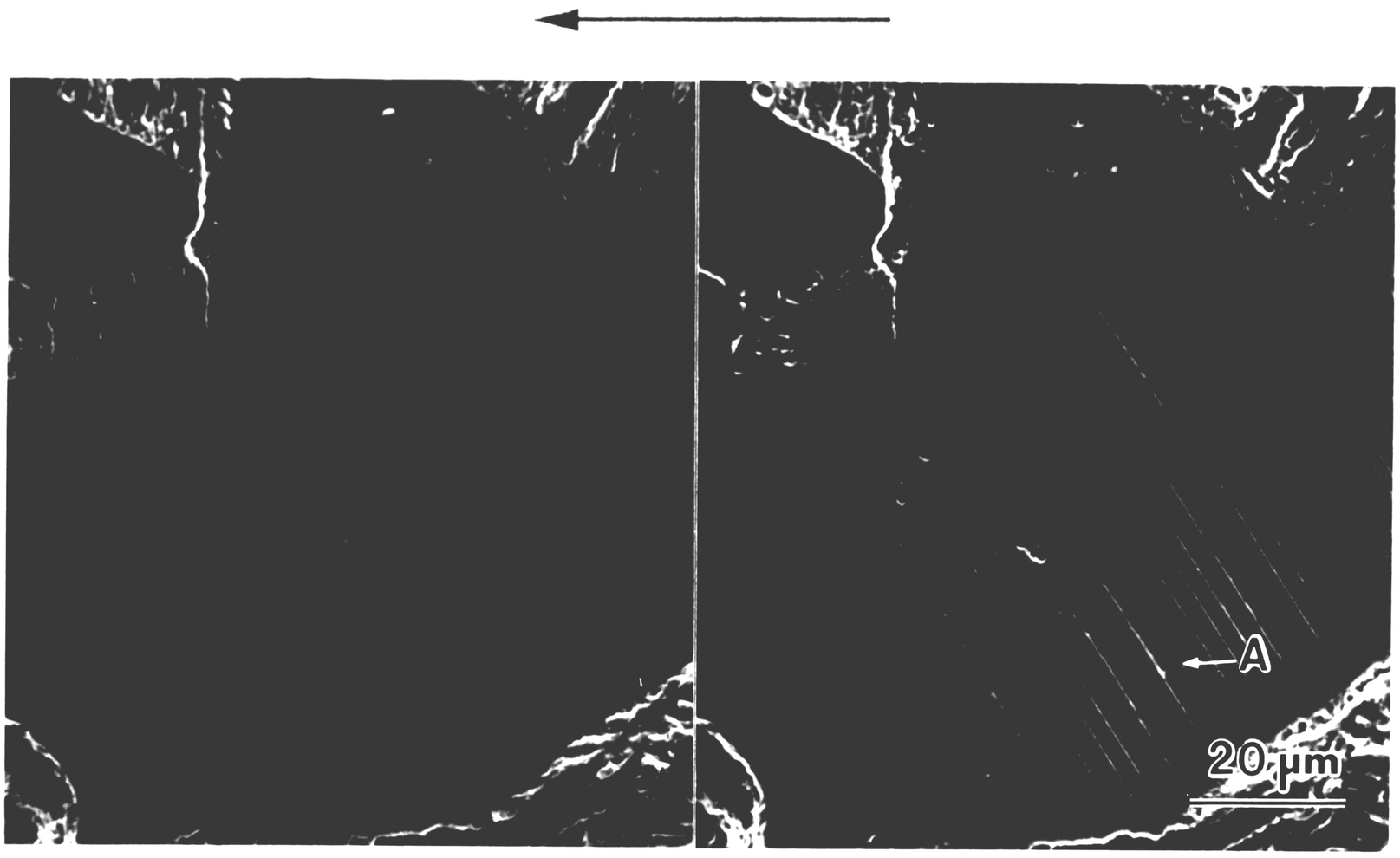

(a) (b)

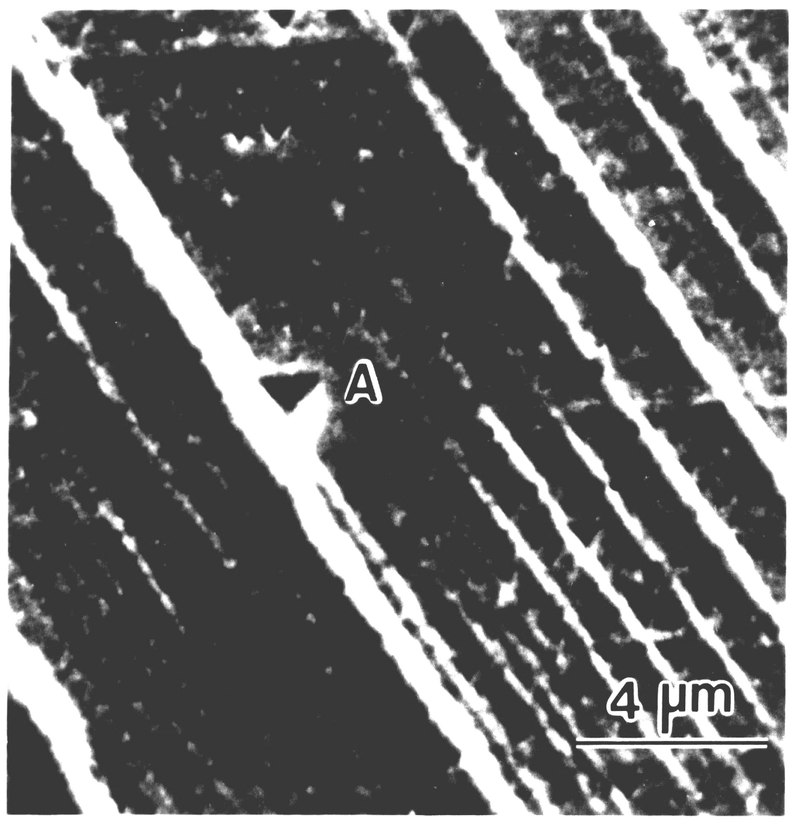

(c)

Fig. 11 SEM microfractographs of annealed 304 stainless steel tested in air at $\Delta K=20$ MPa$\sqrt{m}$, R=0.1 and f=10 Hz, 298 K, showing a facet (a) before etching, (b) after etching, and (c) the facet at high magnification to show the etching pits(Pit A is the pit in region A in (b)).

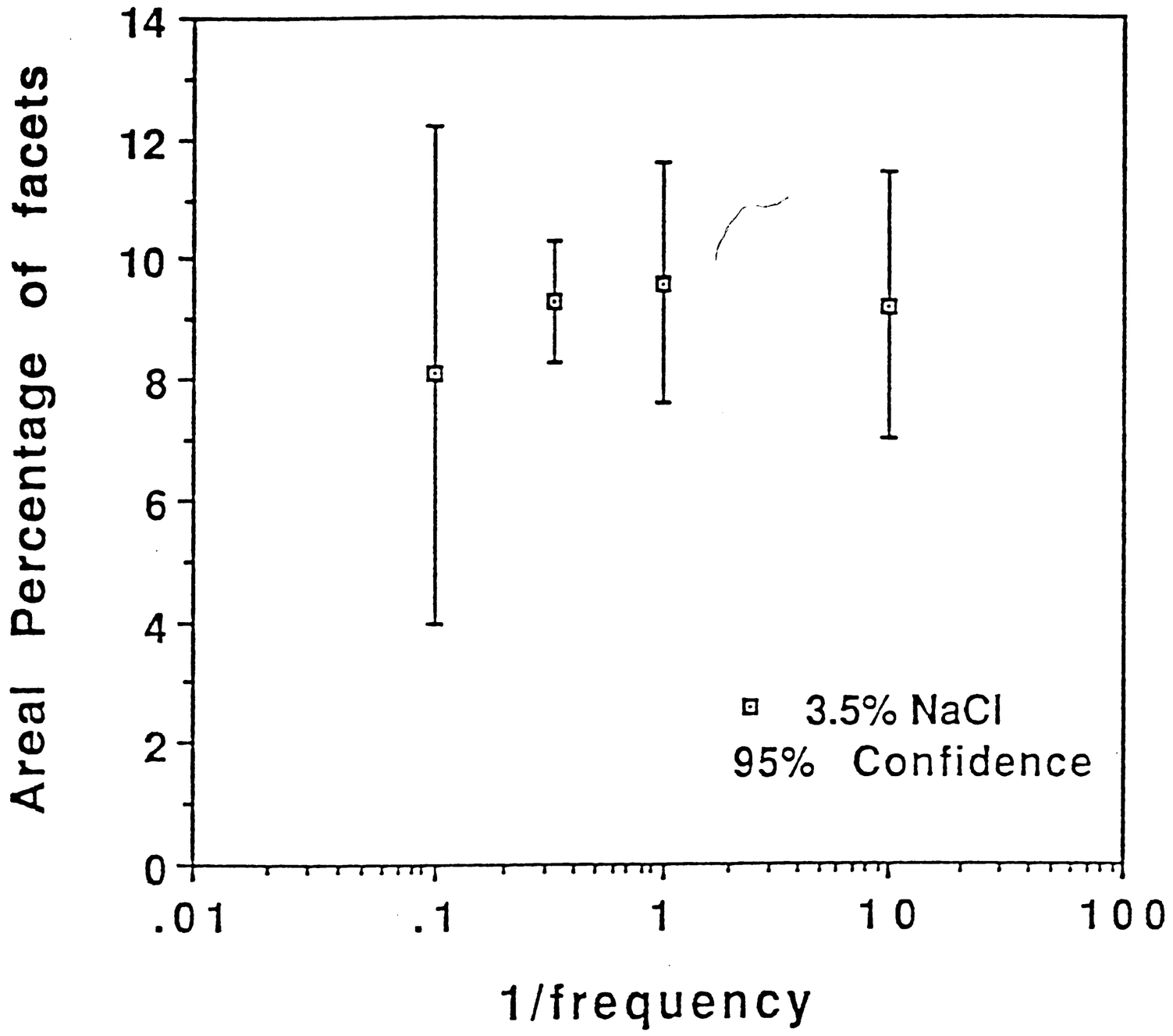

Fig. 12 The areal percentage of facets vs. 1/frequency for an annealed 304 stainless steel tested in 3.5% NaCl solution at ΔK=20 MPa$\sqrt{m}$ and 298 K.

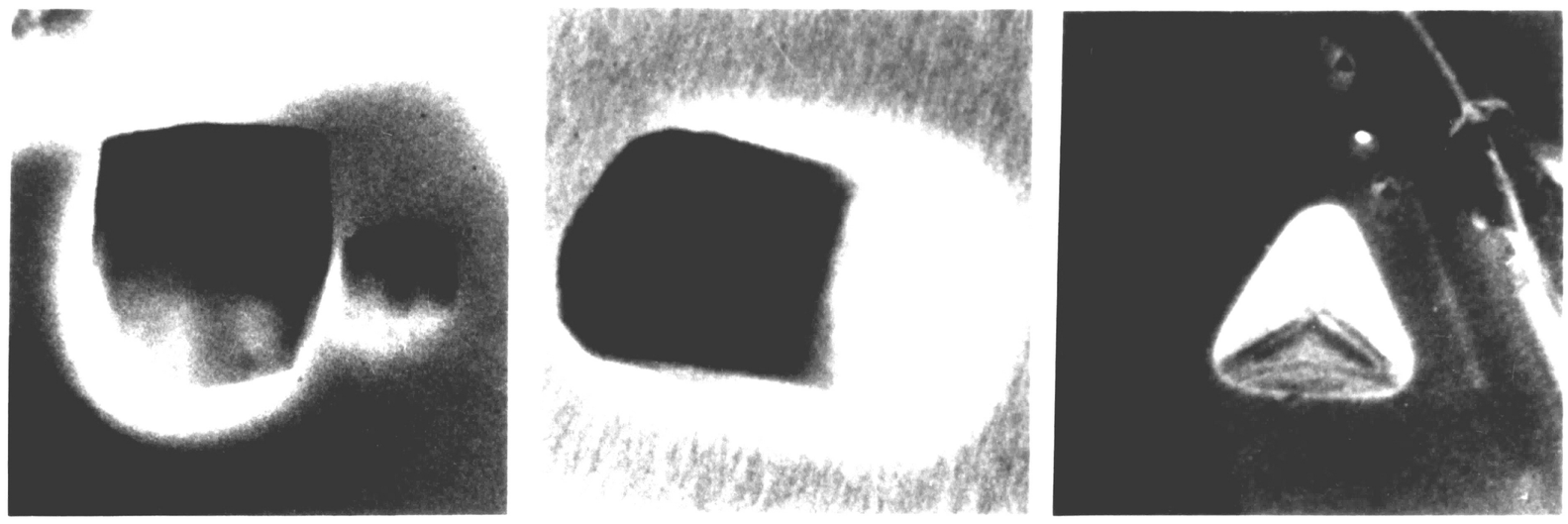

(a)

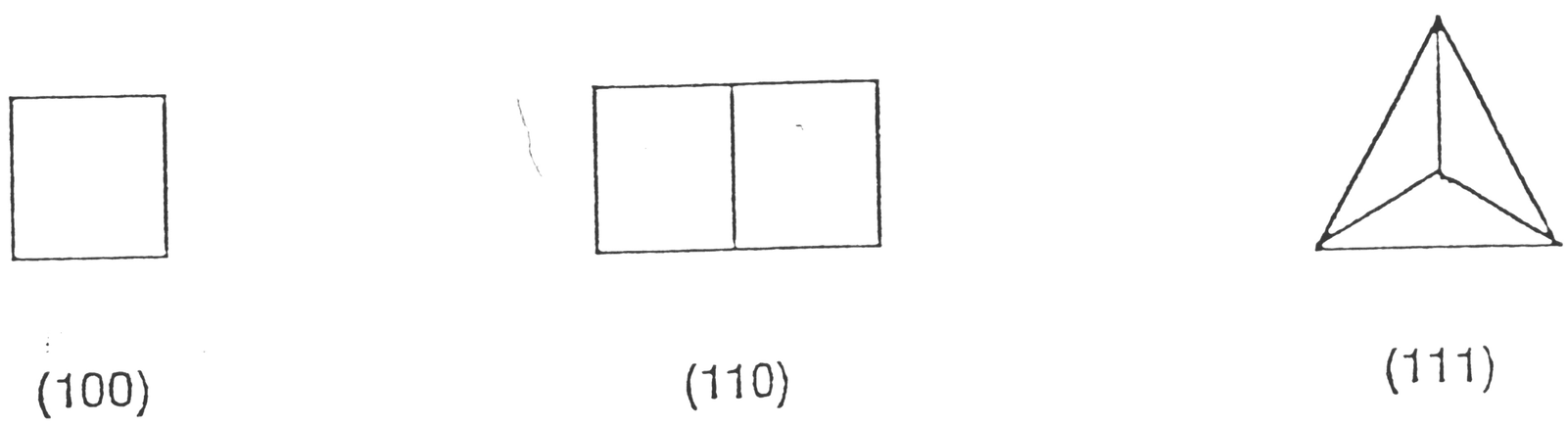

(b)

Fig. 13 Geometric shape of etch pits on {001}, {011} and {111} planes:
(a) SEM micrographs and (b) schematic digrams.
Note: the side faces of etch pits consist of {001} planes.

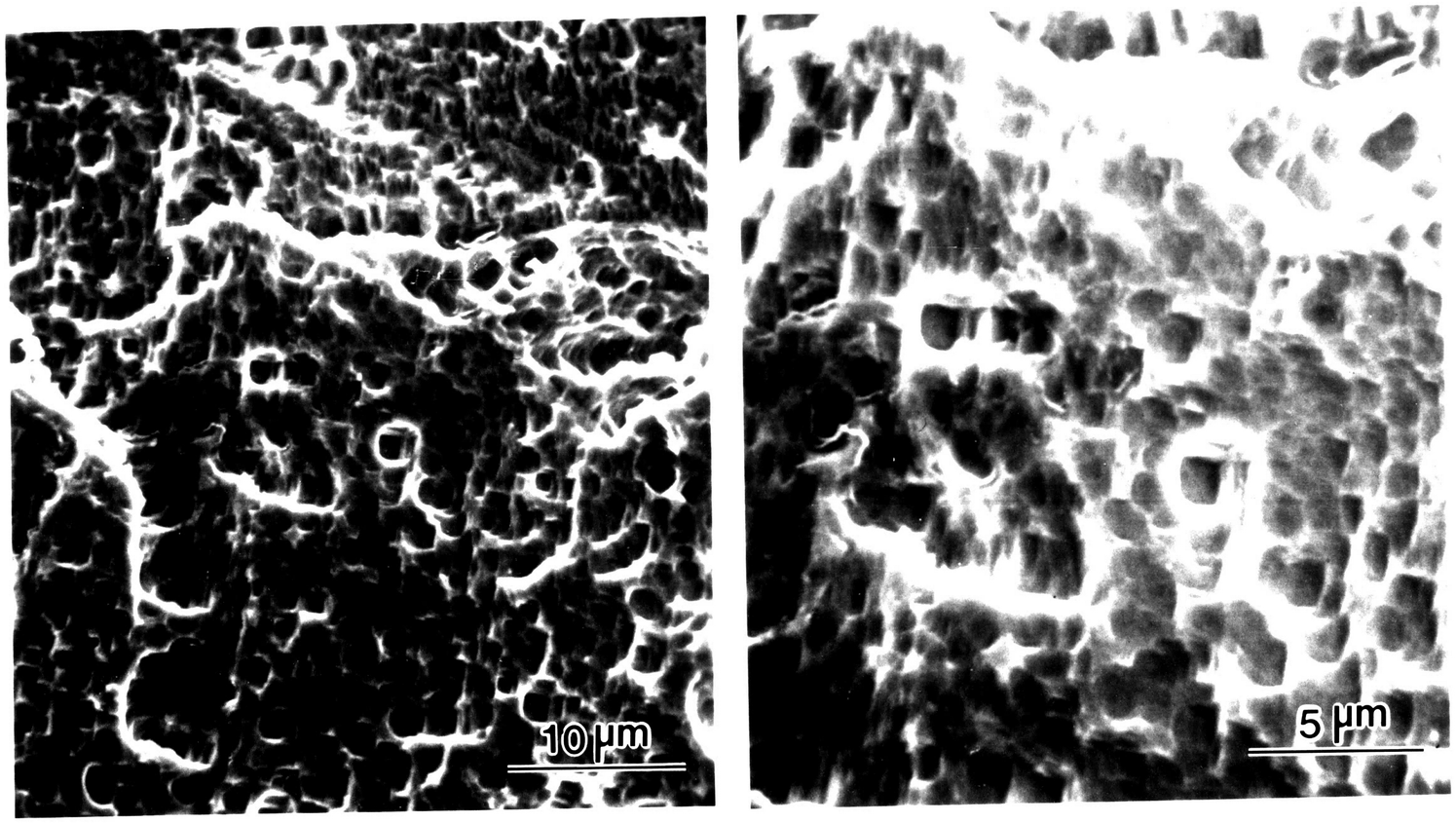

(a) (b)

Fig. 14 SEM microfractographs of annealed 304 stainless steel tested in 3.5% NaCl solution at $\Delta K=20$ MPa$\sqrt{m}$, R=0.1 and f=0.1 Hz, 298 K, showing the quasi-cleavage feature after etching $\{001\}_\gamma$ etch-pits at both (a) low and (b) high magnifications.

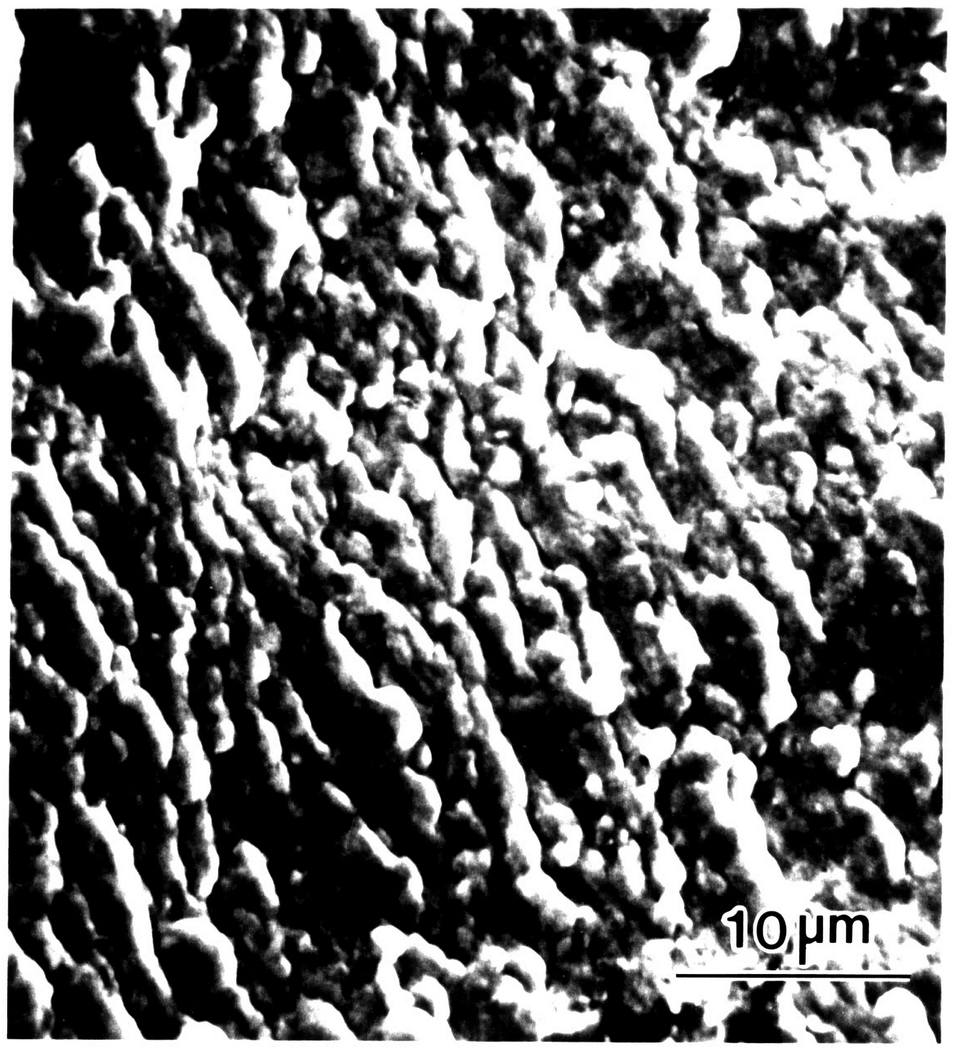

Fig. 15 SEM microfractograph of annealed 304 stainless steel tested in vacuum showing coarse striation-like ductile morphology.

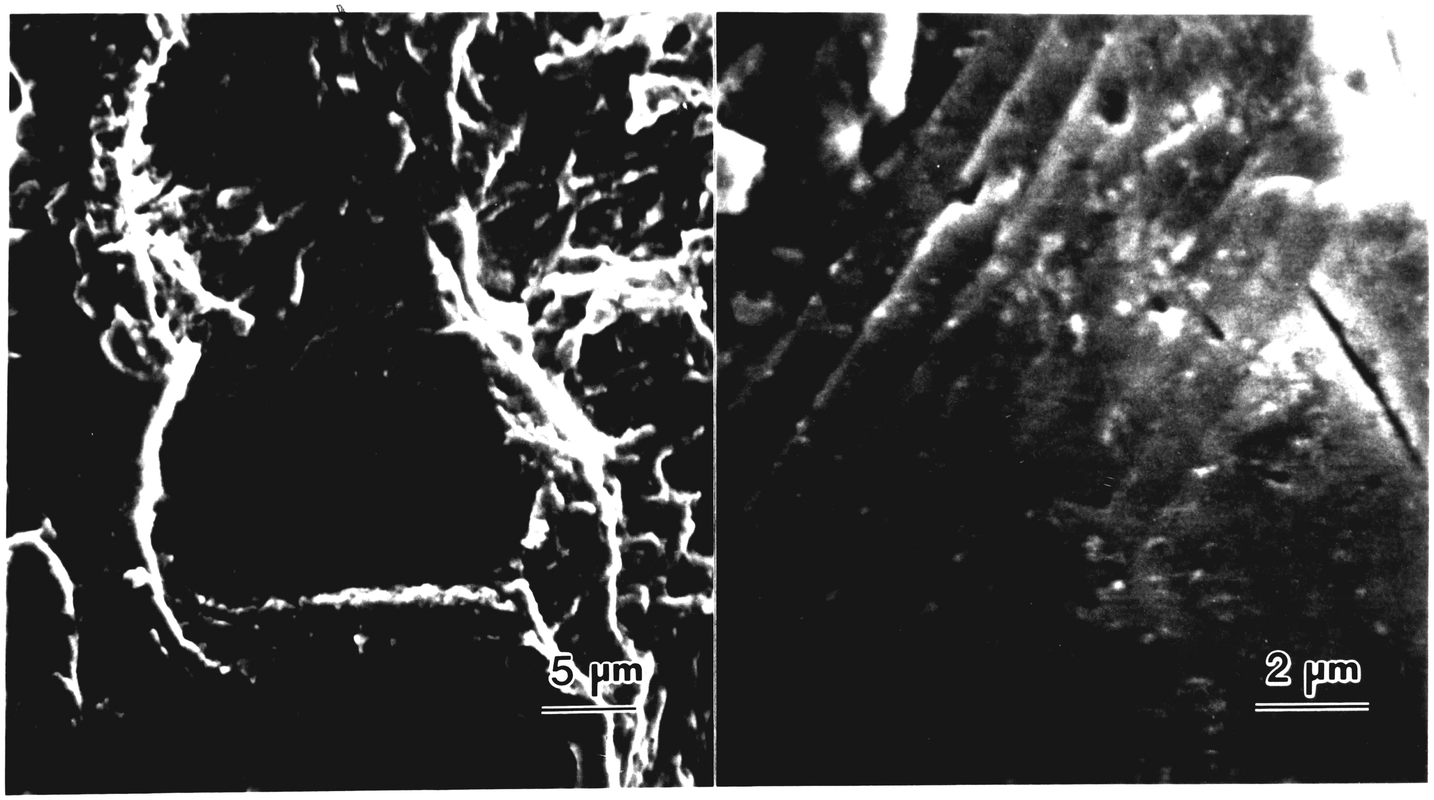

(a) (b)

Fig. 16 SEM microfractograph of cold-rolled 304 stainless steel tested in 3.5% NaCl solution at $\Delta K=30$ MPa$\sqrt{m}$, R=0.1 and f=0.1 Hz, 298 K, showing a facet and its surrounding quasi-cleavage region, and (b) the facet with slip traces at high magnification.

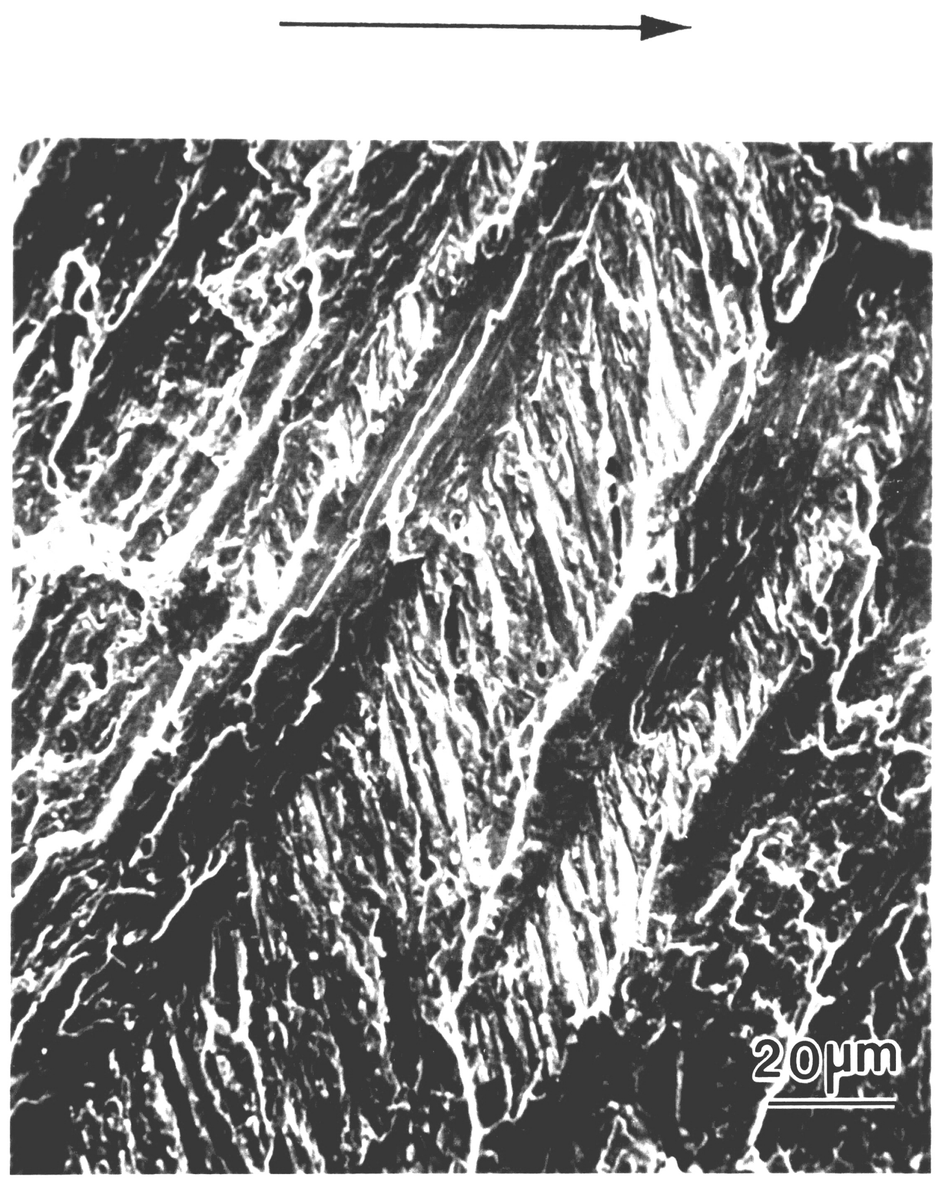

Fig. 17 SEM microfractographs of cold-rolled 304 stainless steel tested in 3.5% NaCl solution at ΔK=30 MPa$\sqrt{m}$, R=0.1, f=10 Hz and 298 K, showing parallel laths in the fracture surface.

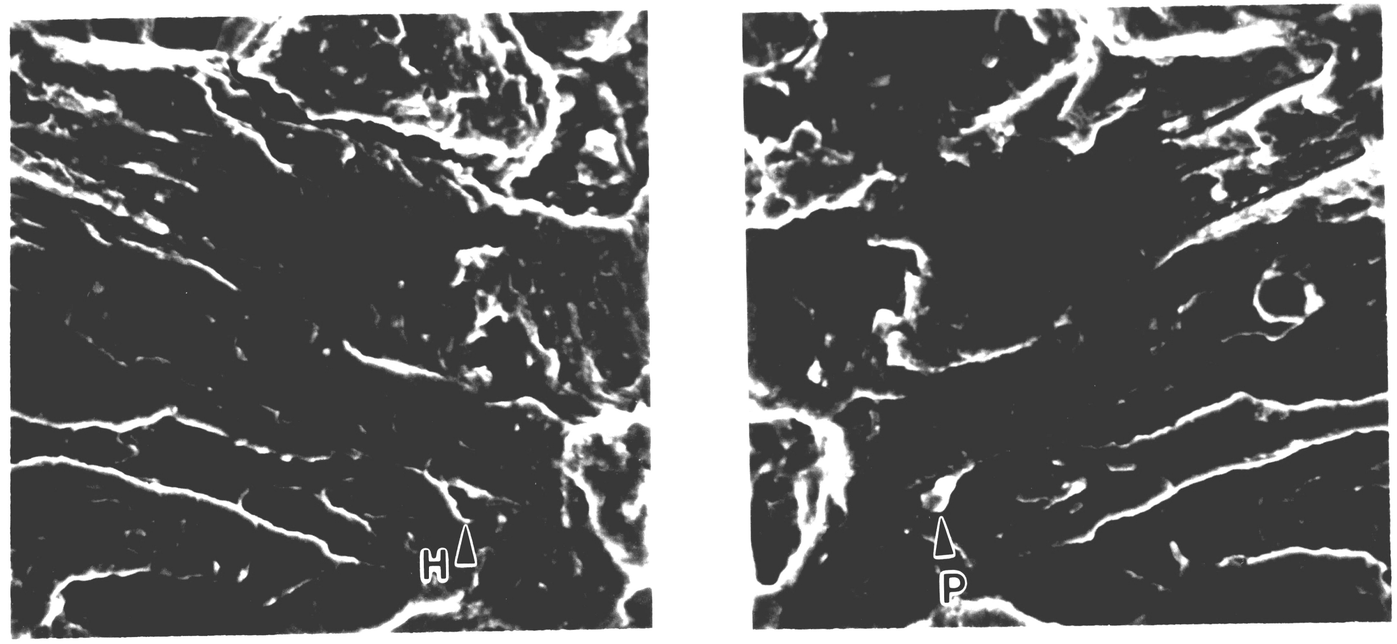

Fig. 18 SEM microfractographs of mating surfaces of cold-rolled stainless steel tested in 3.5% NaCl solution at ΔK=30 MPa$\sqrt{m}$, R=0.1 and f=10 Hz, 298 K, showing a particle-hole pair.

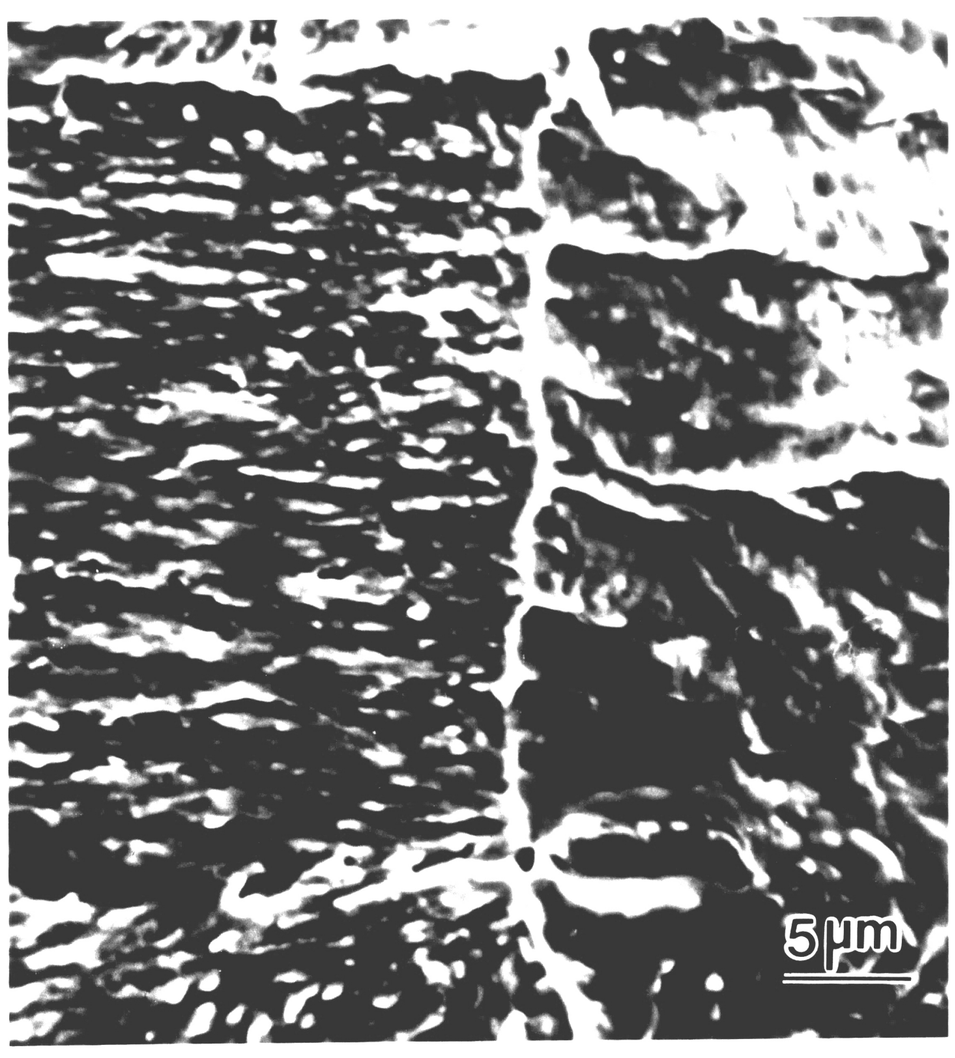

Fig. 19 SEM microfractograph of cold-rolled 304 stainless steel showing a sharp transition in morphology at the border between cracking in vacuum and in air.

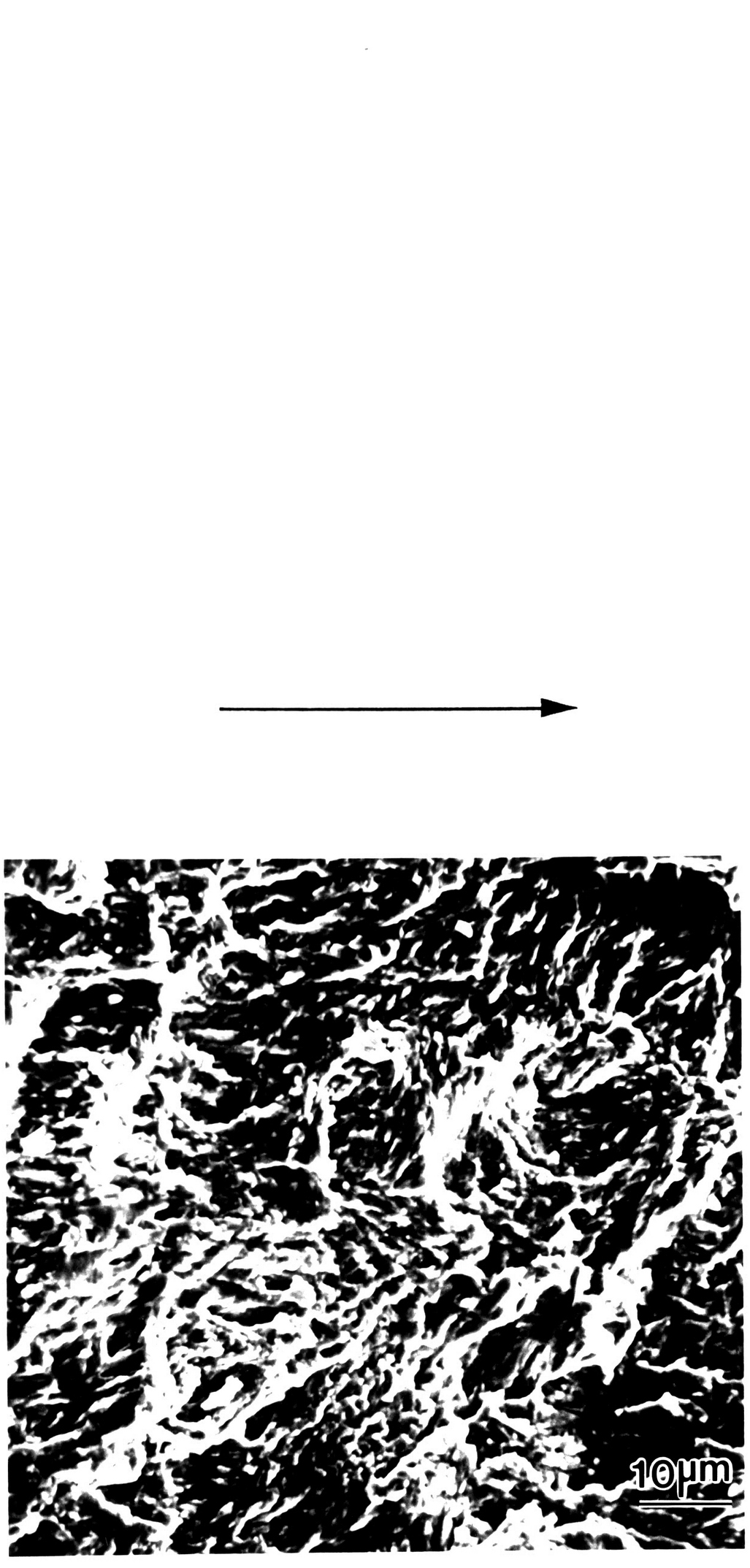

Fig. 20 SEM microfractograph of cold-rolled 304 stainless steel tested in vacuum showing ductile nature of the fracture surface morphology.

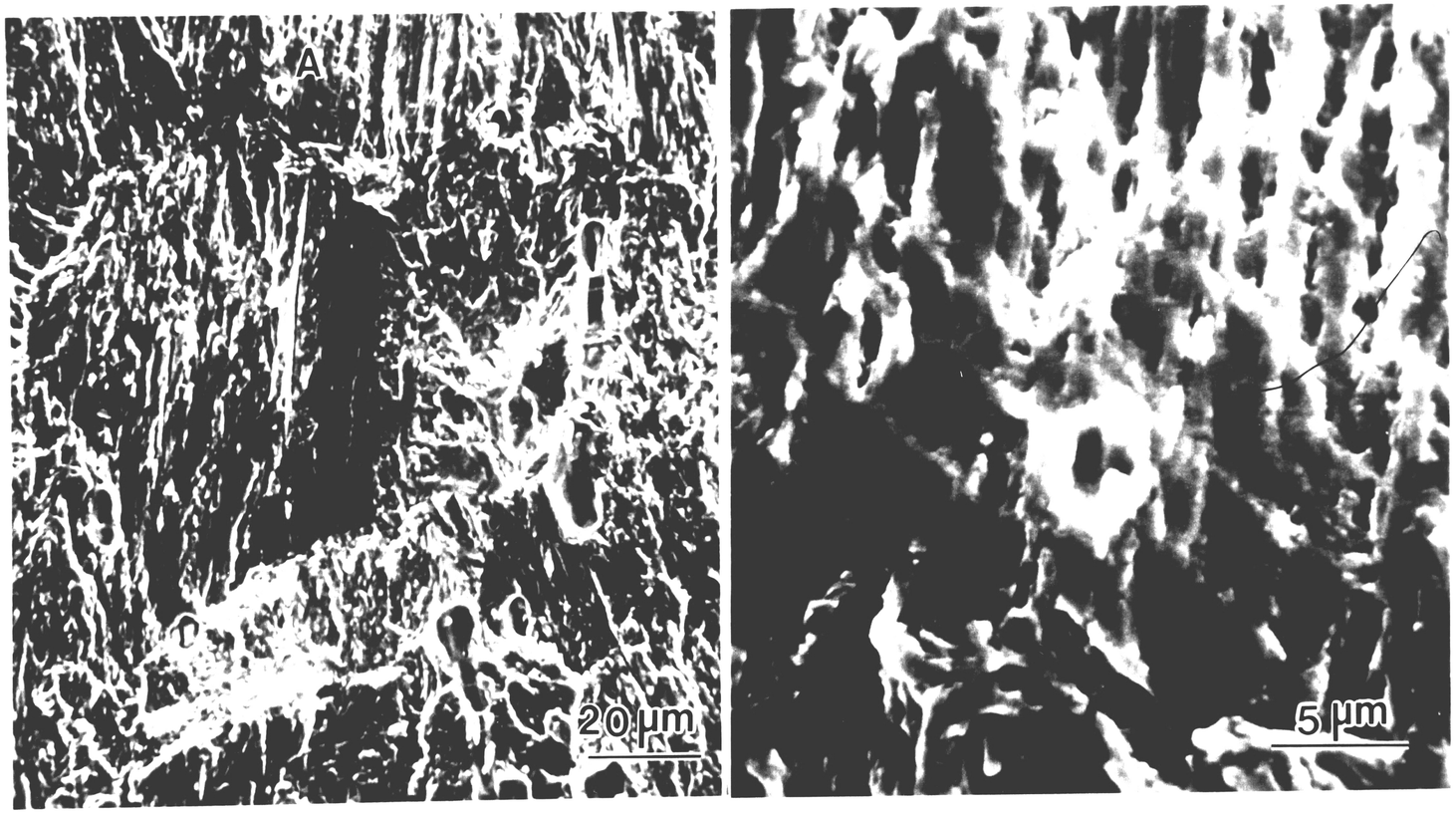

(a) (b)

Fig. 21 SEM microfractographs of cold-rolled 304 stainless steel tested in vacuum showing the slip traces in (b) as marked by A in (a).

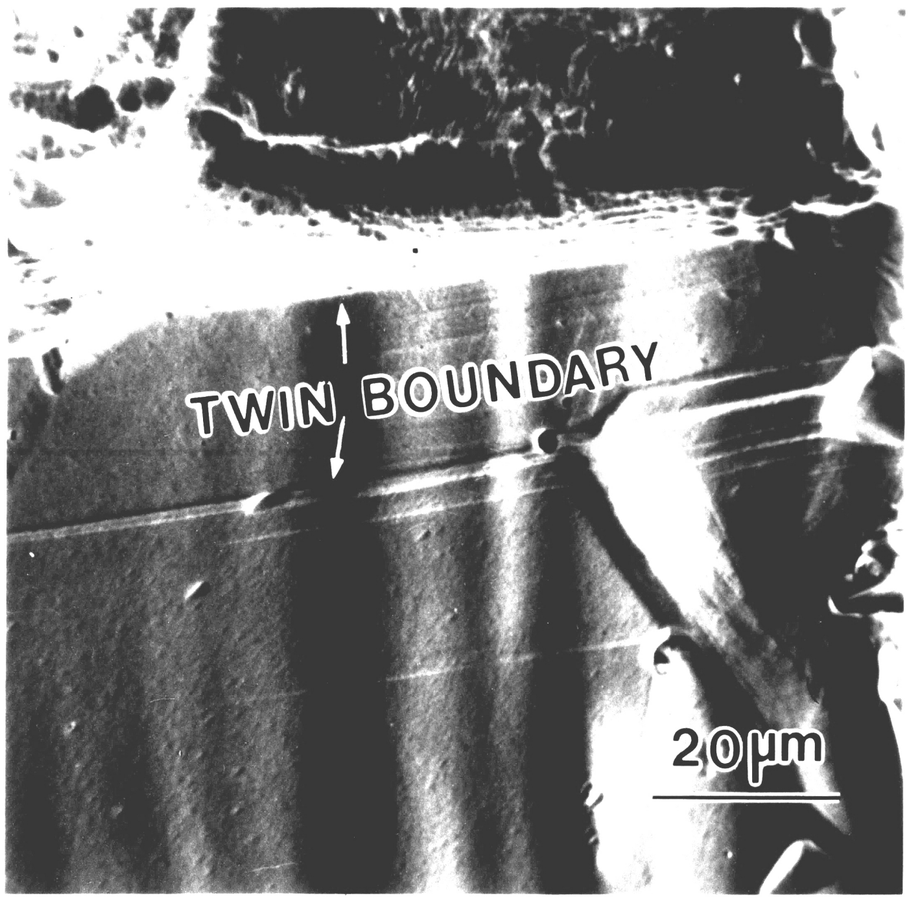

Fig. 22 SEM microfractograph of annealed 304 stainless steel tested in 3.5% NaCl solution at $\Delta K=20$ MPa$\sqrt{m}$, R=0.1 and f=10 Hz, 298 K, showing a fracture facet formed along a twin boundary.
(transverse section of the fracture surface)

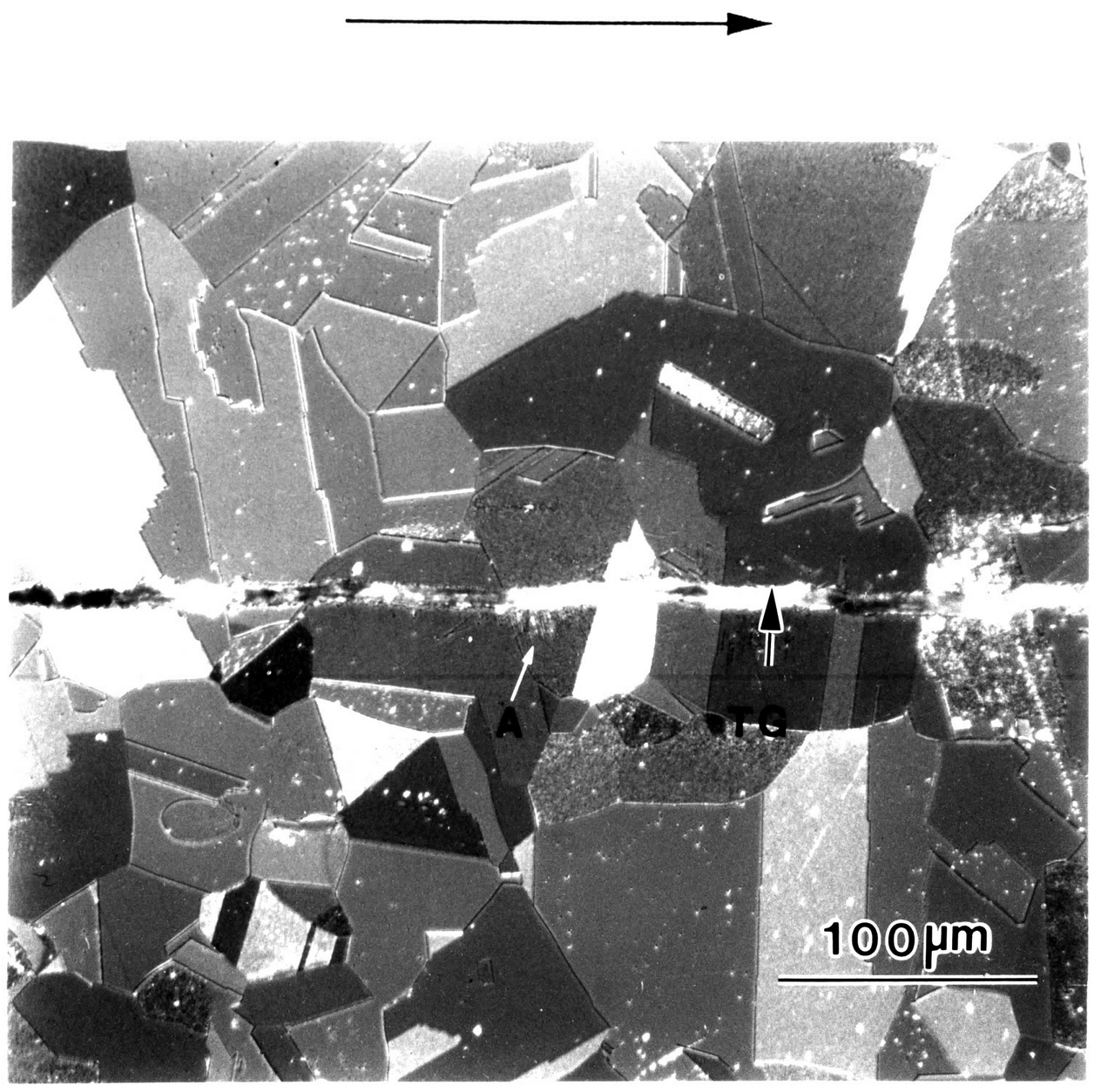

Fig. 23 Crack path at the midsection of an annealed 304 stainless steel specimen which was tested in air, showing transgranular (TG) separation and slip bands(for example at A).

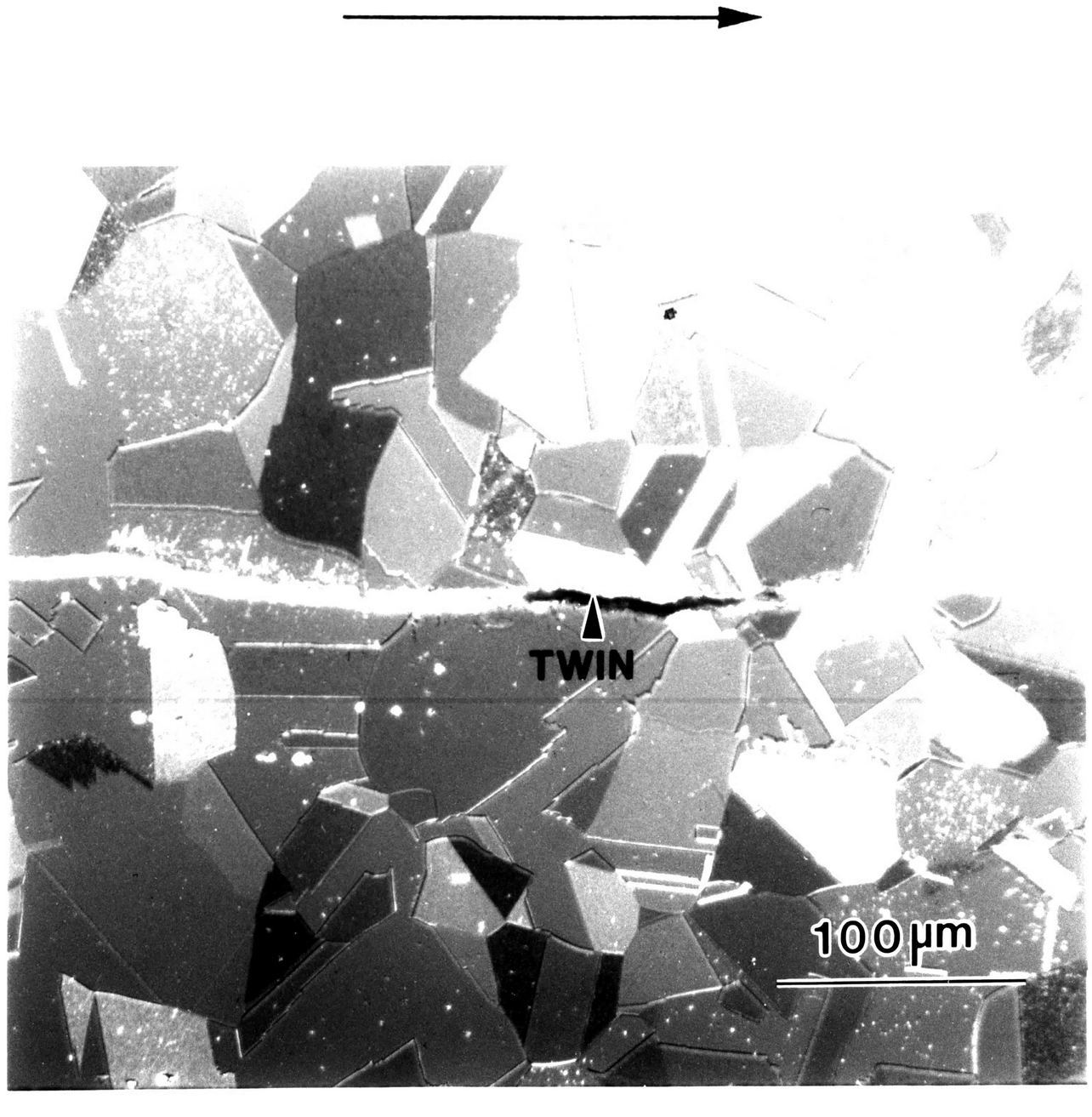

Fig. 24 Crack path at the midsection of an annealed 304 stainless steel specimen which was tested in air, showing separation along a twin boundary.

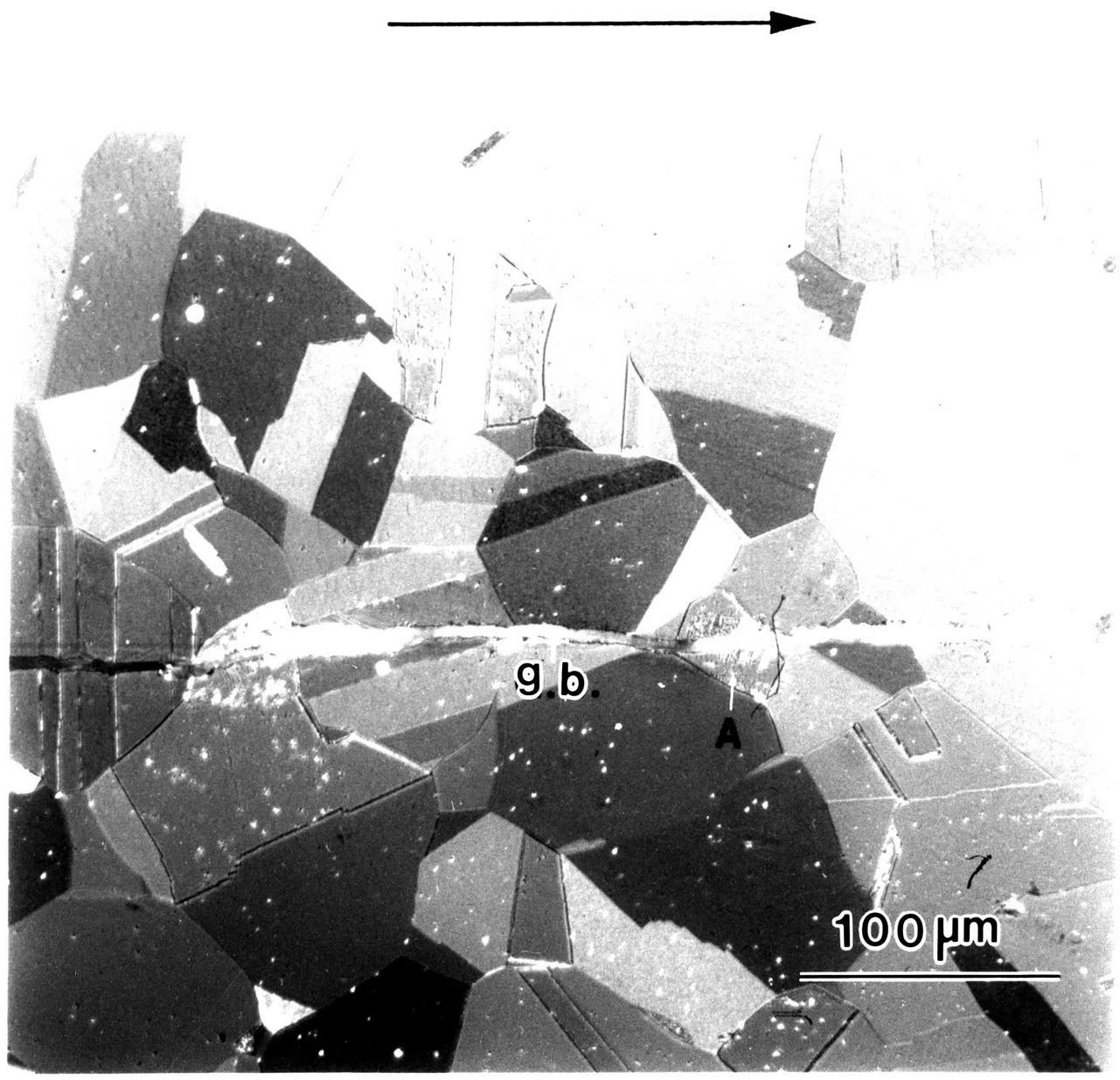

Fig. 25 Crack path at the midsection of an annealed 304 stainless steel specimen which was tested in air, showing separation along a grain boundary and slip bands at A.

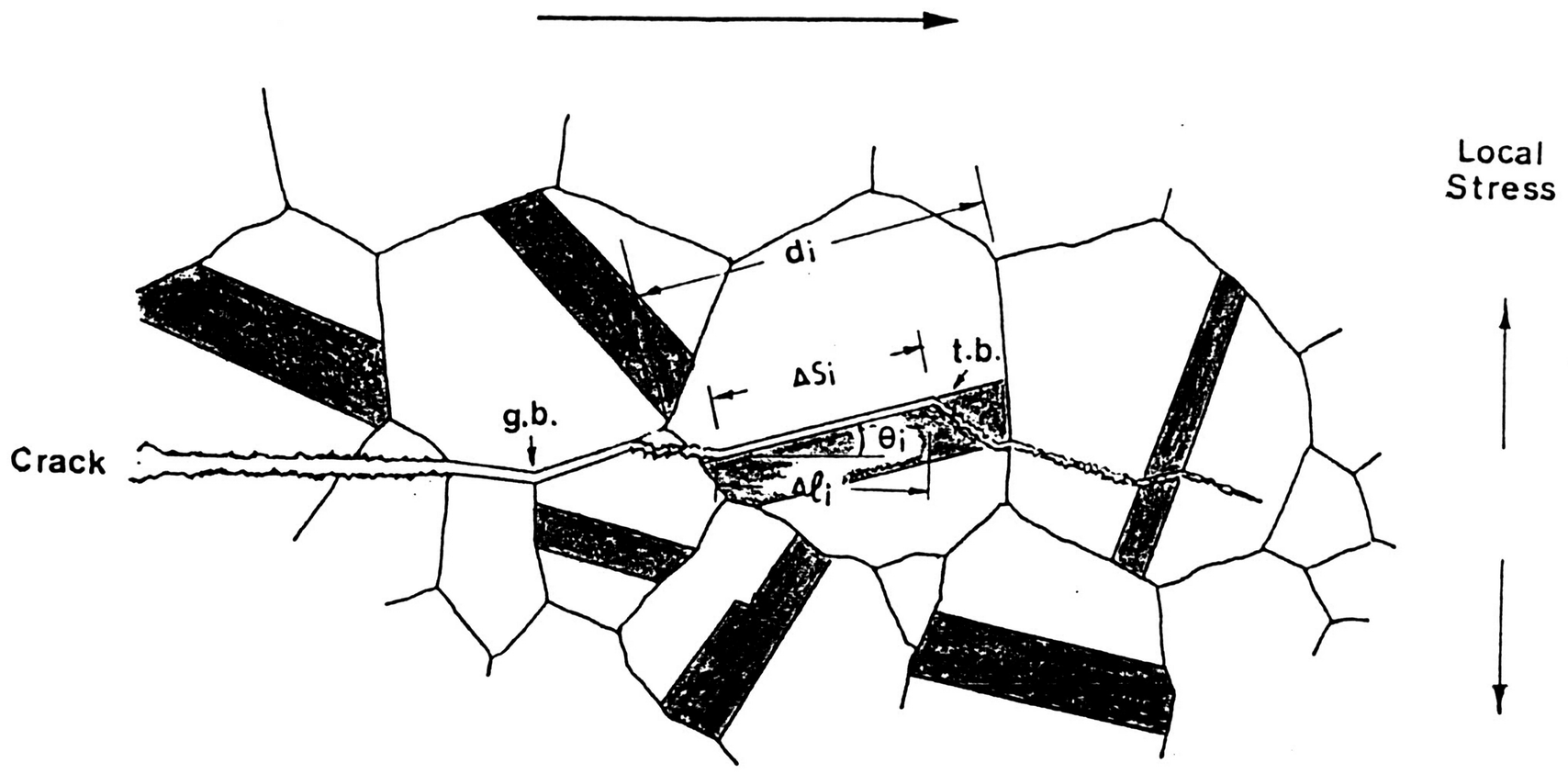

Fig. 26 A schematic diagram of crack paths in annealed 304 stainless steel, showing the cracking across grains(transgranular) and along twin and grain boundaries.
(g.b. stands for grain boundary separation, t.b. for twin boundary cracking)

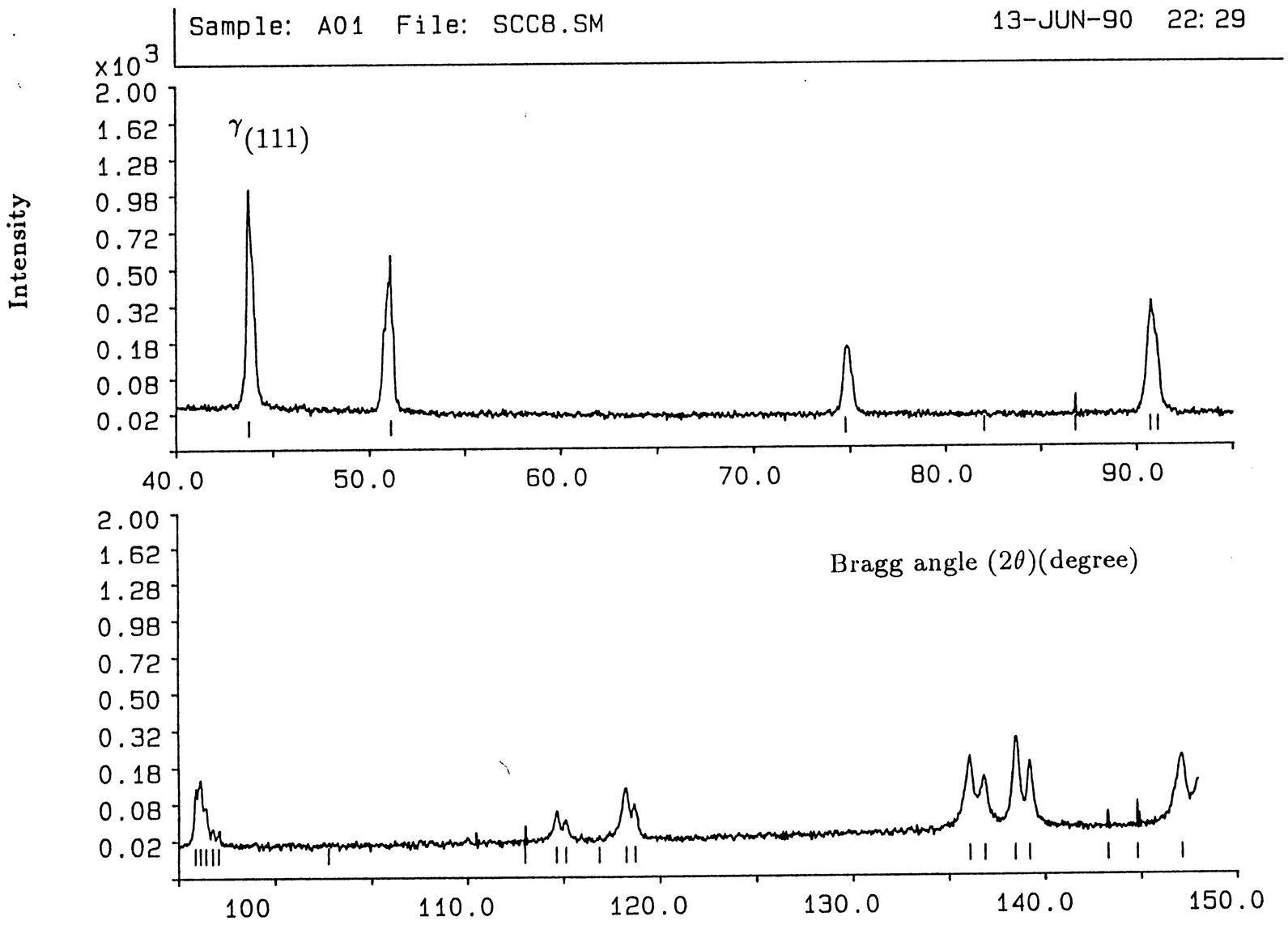

Fig. 27 X-ray diffraction pattern of an annealed 304 stainless steel specimen which was ground, polished and electroetched.

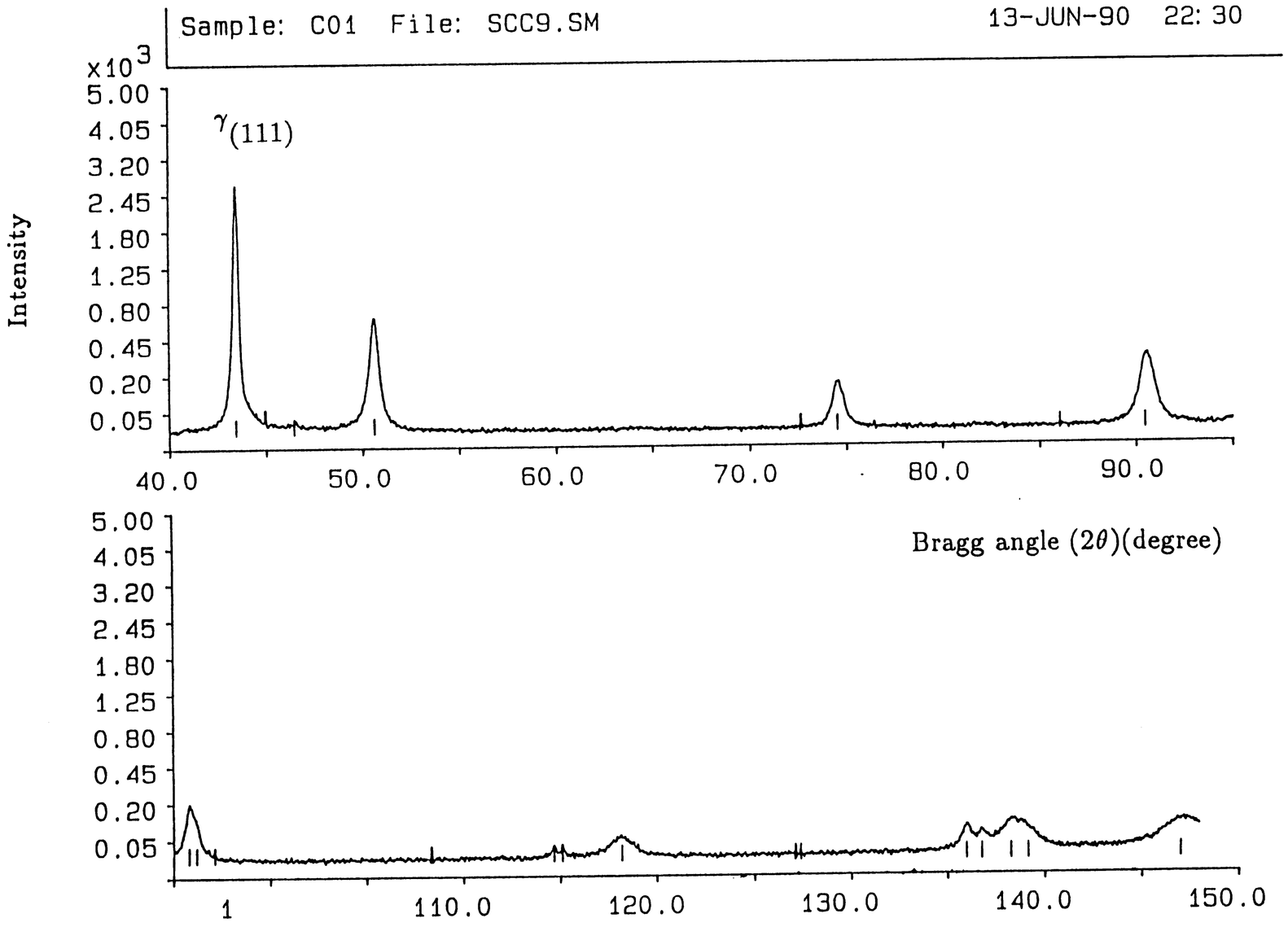

Fig. 28 X-ray diffraction pattern of a cold-rolled 304 stainless steel specimen which was ground, polished and electroetched.

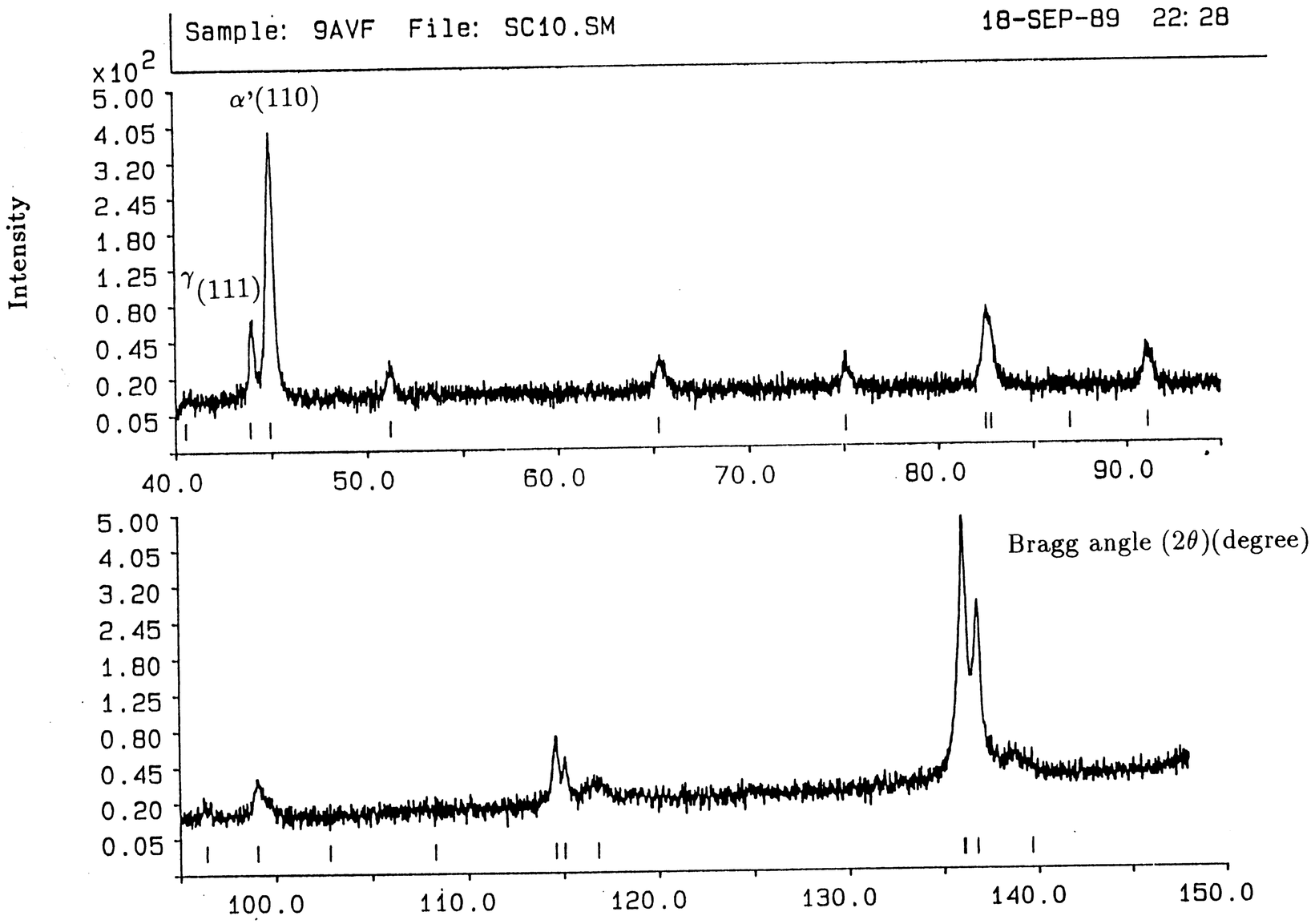

Fig. 29 X-ray diffraction pattern of fracture surface of an annealed 304 stainless steel tested in vacuum at a constant ΔK of 24 MPa$\sqrt{m}$.

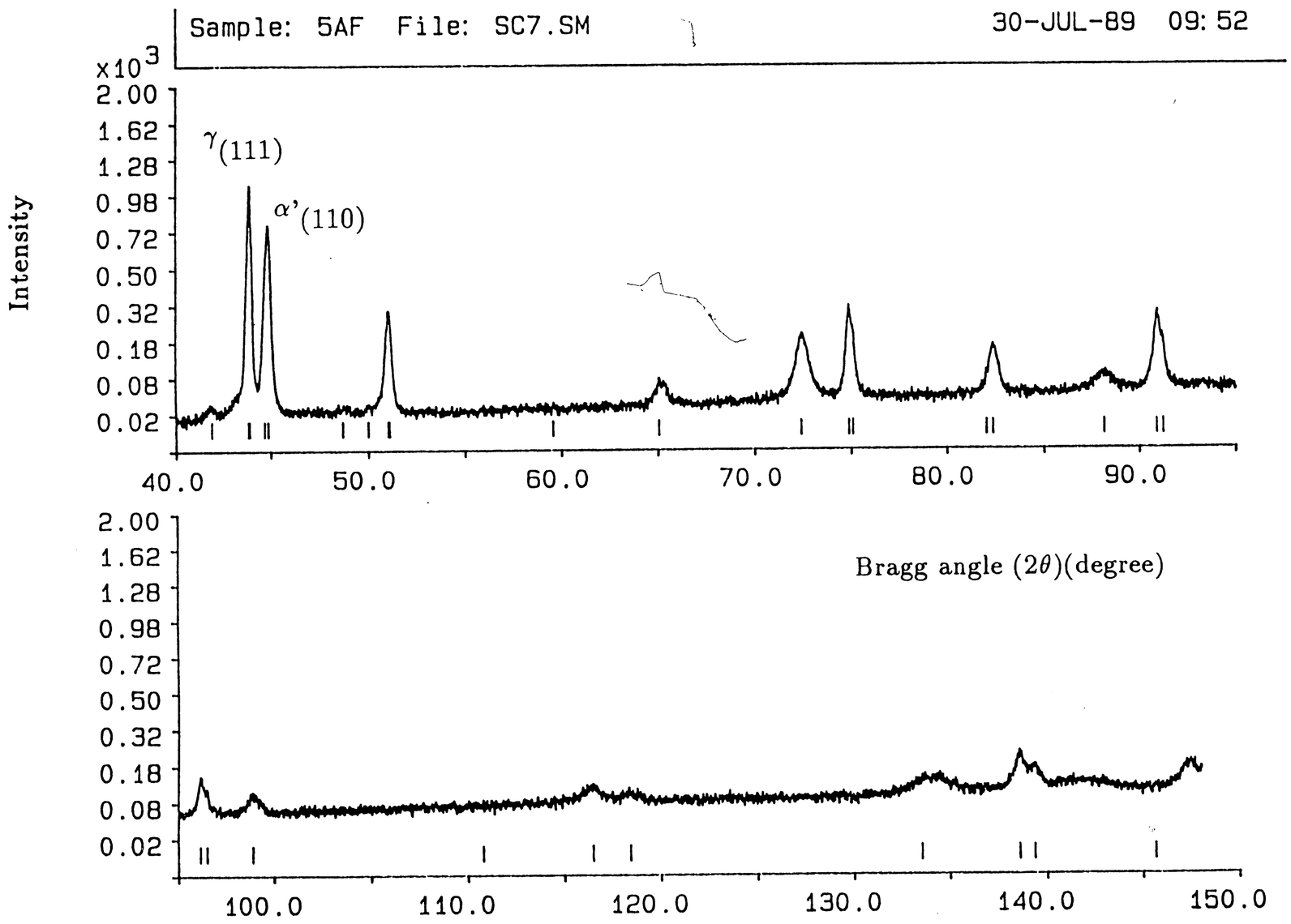

Fig. 30 X-ray diffraction pattern of fracture surface of an annealed 304 stainless steel tested in air at a constant ΔK of 20 MPa$\sqrt{m}$.

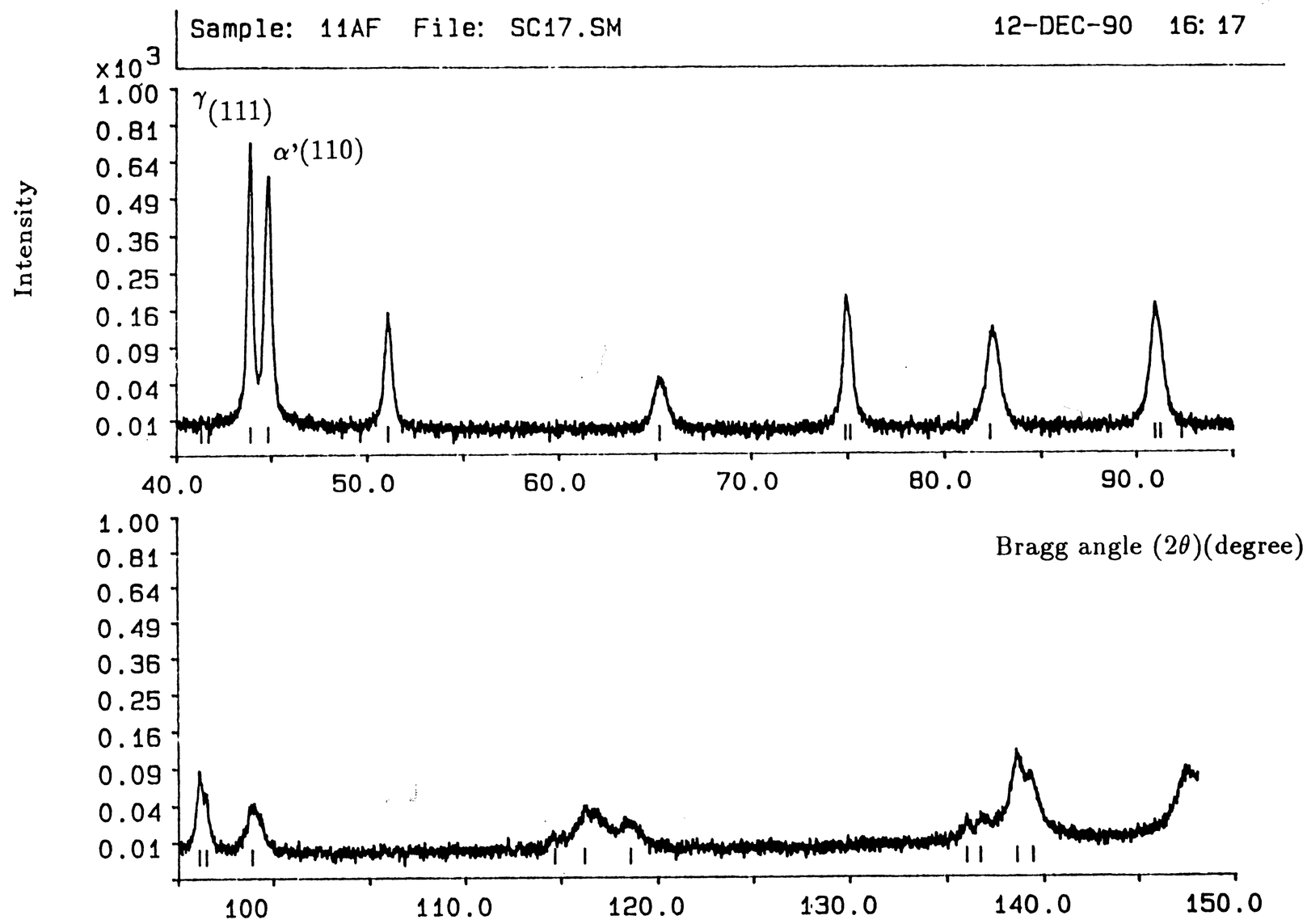

Fig. 31 X-ray diffraction pattern of fracture surface of an annealed 304 stainless steel tested in 3.5% NaCl solution at a constant ΔK of 20 MPa$\sqrt{m}$.

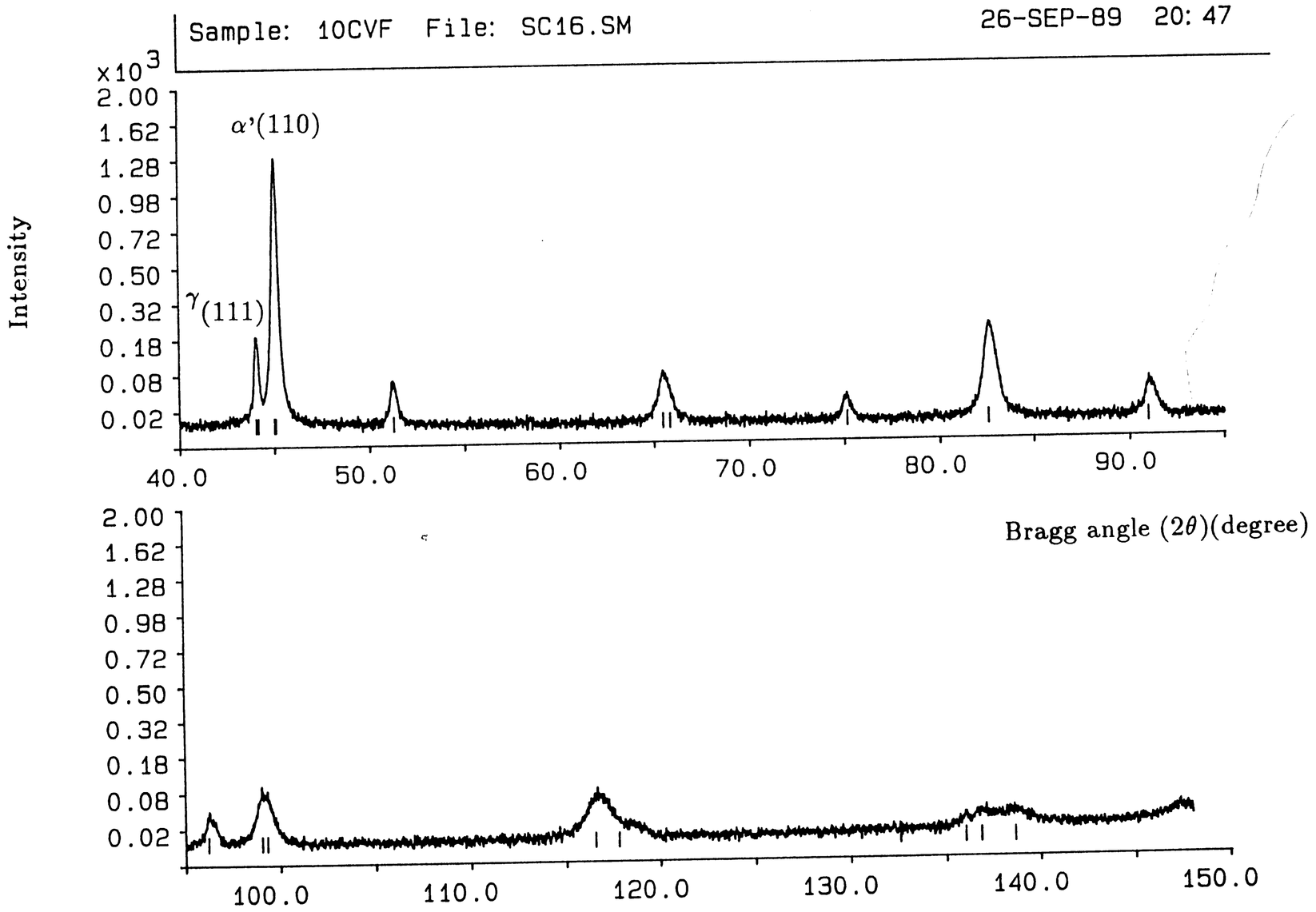

Fig. 32 X-ray diffraction pattern of fracture surface of a cold-rolled 304 stainless steel tested in vacuum at a constant ΔK of 20 MPa$\sqrt{m}$.

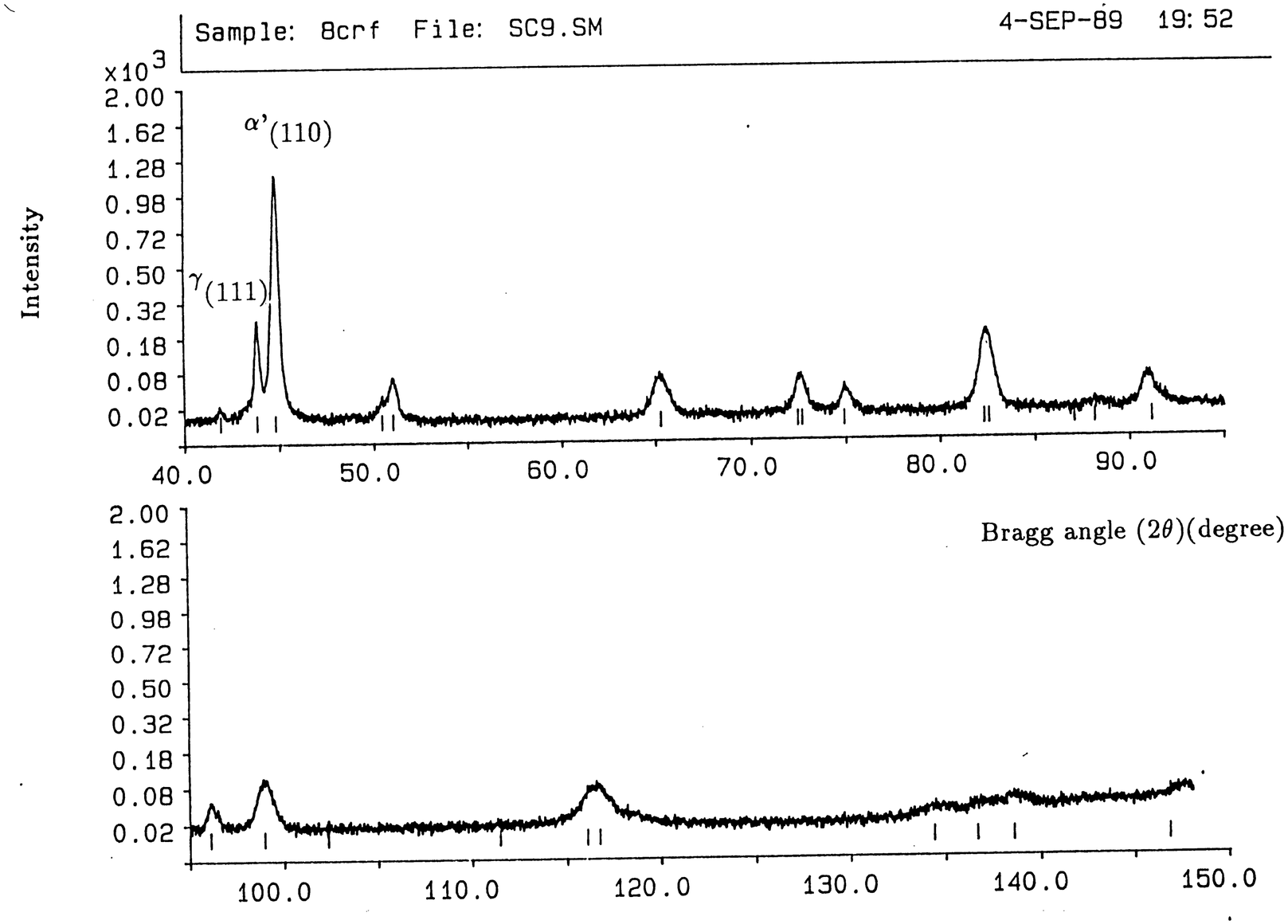

Fig. 33 X-ray diffraction pattern of fracture surface of a cold-rolled 304 stainless steel tested in air at a constant ΔK of 20 MPa$\sqrt{m}$.

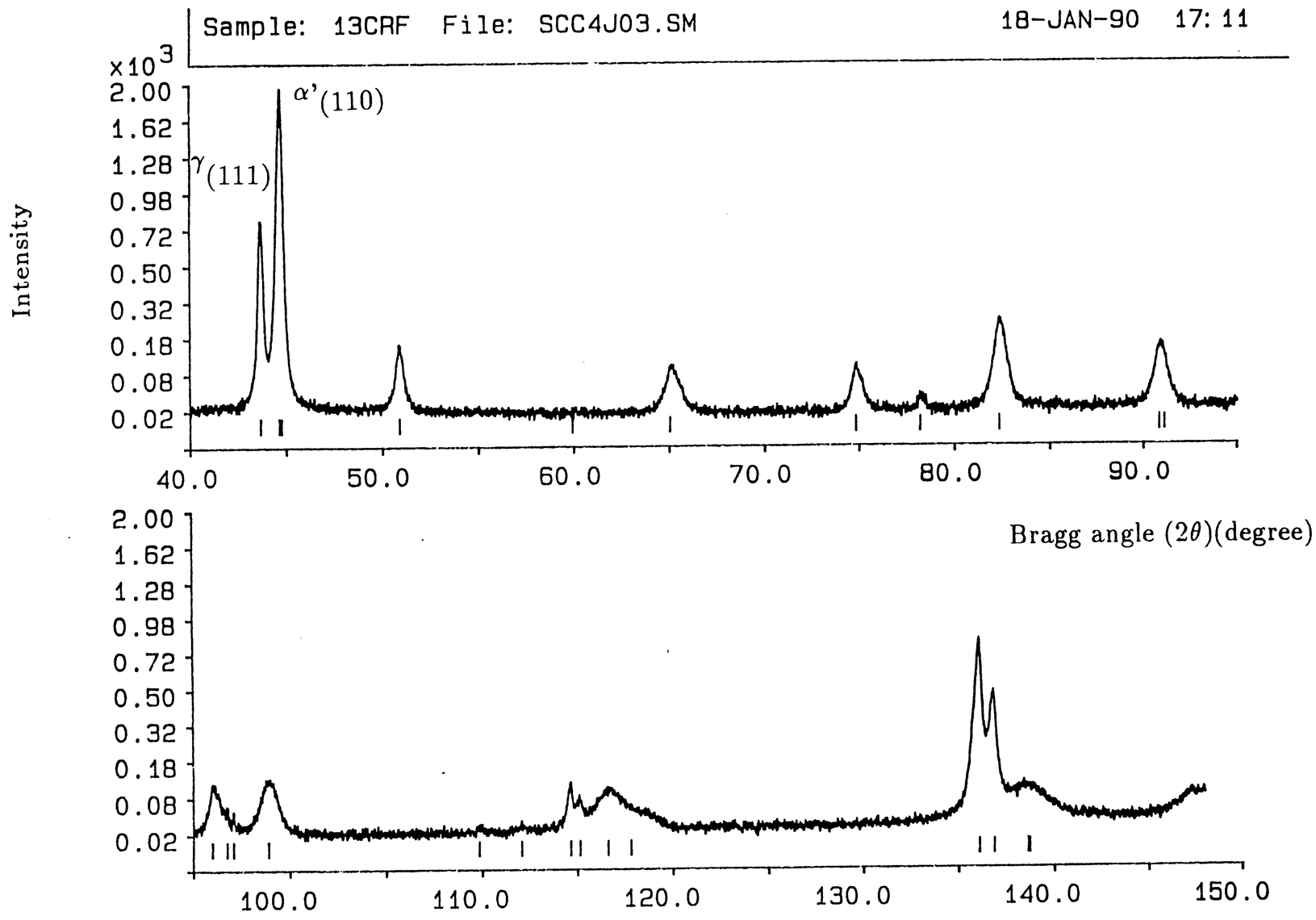

Fig. 34 X-ray diffraction pattern of fracture surface of a cold-rolled 304 stainless steel tested in 3.5% NaCl solution at a constant ΔK of 20 MPa$\sqrt{m}$.

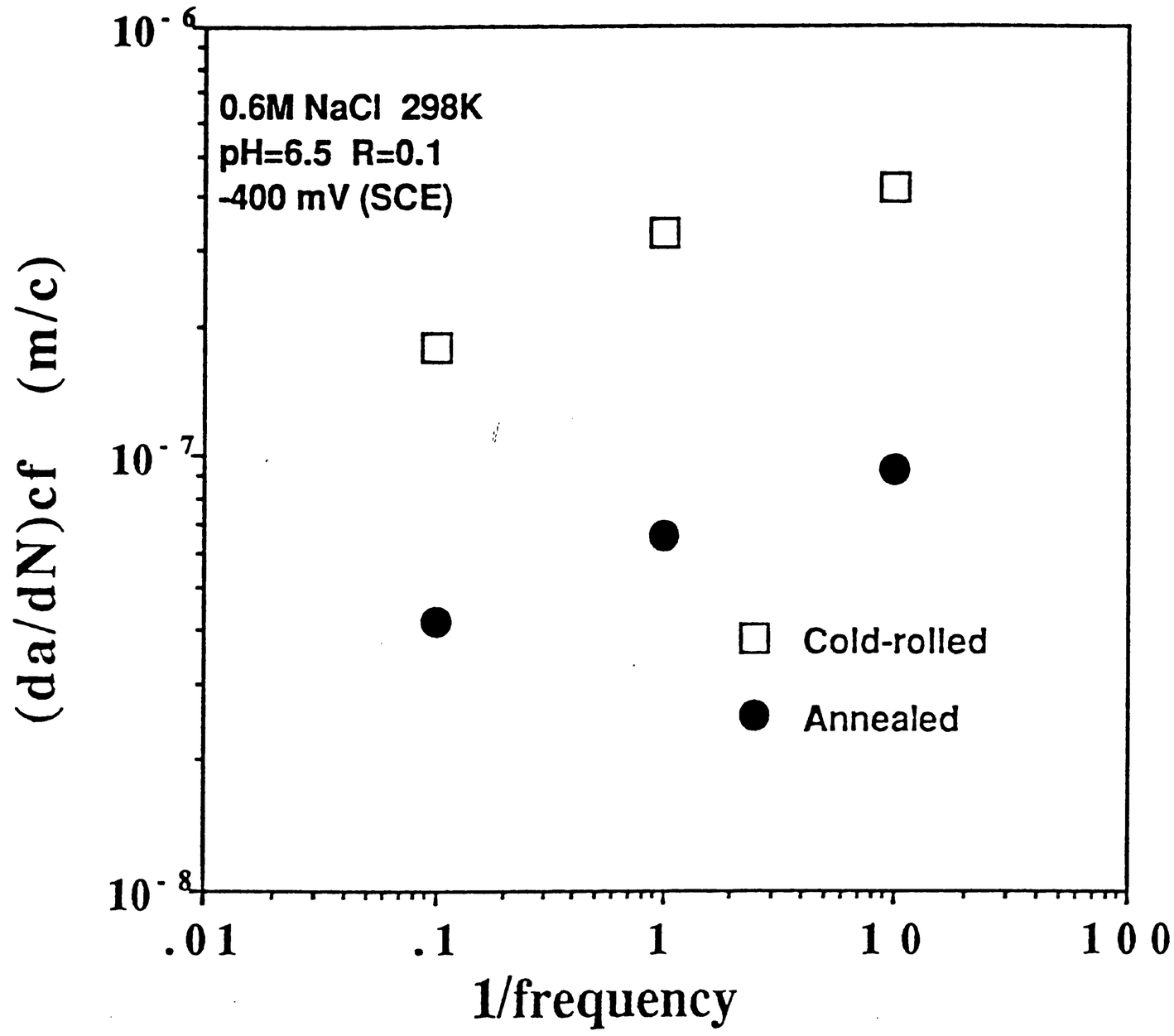

Fig. 35 Corrosion fatigue crack growth rate as a function of 1/frequency in cold-rolled and annealed 304 stainless steels at a constant ΔK of 20 MPa$\sqrt{m}$.

References:

[1] D. E. Allison, "The Interaction of Crack Geometry and Electrochemical Processes in Corrosion Fatigue of AISI 304 Stainless Steel", PH.D. Disseration, Department of Mechanical Engineering and Mechanics, Lehigh University, Bethlehem, PA.

[2] J. I. Dickson, D. Groulx and Li Shiqiong, "The Fractography of Stress CorrosionCracking of 310 Stainless Steel: Crystallographic Aspects and The Influence of The Stress Intensity Factor", Materials Sci. & Eng. , 94, 1987, pp. 155-173.

[3] R. Liu, N. Narita, C. Altstetter, H. Birnbaum and E. N. Pugh, "Studies of The Orientations of Fracture Surfaces Produced in Austenitic Stainless Steels By Stress-Corrosion Cracking and Hydrogen Embrittlement", Metall. Trans. A, 11A, Sept. 1980, pp. 1563-1574.

[4] E. I. Meletis and R. F. Hochman, "The Crystallography of Stress-Corrosion Cracking in Face Centered Cubic Single Crystals", Corrosion Sci. , Vol. 24, No. 10, 1984, pp. 843-862.

[5] Y. Mukai, M. Watanabe and M. Murata, "Fractographic Observation of Stress- Corrosion Cracking of AISI 304 Stainless Steel in Boiling 42 Percent Magnesium-Chloride Solution" Fractography in Failure Analysis, ASTM STP 645, B. M. Strauss and W. H. Cullen, Jr. , Eds., 1978, pp. 164-175.

[6] D. Hennessy, G. Steckel and C. Altstetter, "Phase Transformation of Stainless Steel During Fatigue", Metall. Trans. A, 7A, March 1976, pp. 415-424.

[7] G. Schuster and C. Altstetter, "Fatigue of Annealed and Cold Worked Stable and Unstable Stainless Steels", Metall. Trans. A, 14A, Oct. 1983, pp. 2077-2084.

[8] G. Schuster and C. Altstetter, "Fatigue of Stainless Steel in Hydrogen", Metall. Trans. A, 14A, Oct. 1983, pp. 2085-2090.

[9] C. L. Briant, "Hydrogen Assisted Fracture in FCC Metals and Alloys", Hydrogen Effects in Metals, I. M. Bernstein and A. M. Thompson, Eds., 1980, pp. 541-553.

[10] R. P. Wei and M. Gao, "Reconsideration of The Superposition Model For Environmentally Assisted Fatigue Crack Growth", Scripta Metallurgica, Vol. 17, 1983, pp. 959-962.

[11] E. L. Meletis and R. F. Hochman, "Techniques for Determination of The Crystallographic Characteristics of Environmentally Induced Brittle Fractures", J. of Testing and Evaluation, Vol. 12, No. 3, May 1984, pp. 142-148.

[12] R. B. Benson, Jr. , R. K. Dann and L. W. Roberts, Jr. , "Hydrogen Embrittlement of Stainless Steel", Trans. AIME, Vol. 242, 1968, pp. 2199-2205.

[13] R. M. Vennett and G. S. Ansell, "A Study of Gaseous Hydrogen Damage in Certain FCC Metals", Trans. ASM, Vol. 62, 1969, pp. 1007-1013.

[14] D. Eliezer, D. G. Chakrapani, C. Altstetter and E. N. Pugh, Proc. 2nd International Congress on Hydrogen in Metals, France, Paris, June 6-11, Pergamon Press, Paris, Paper 3F5, 1977.

[15] P. R. Rhodes, "Mechanism of Chloride Stress Corrosion Cracking of Austenitic Stainless Steels", Corrosion, Vol. 25, No. 11, Nov. 1969, pp. 46-472.

[16] R. P. Reed, "The Spontaneous Martensitic Transformations in 18% Cr, 8% Ni Steels", Acta Metallurgica, Vol. 10, Sept. 1962, pp. 865-877.

[17] J. F. Breedis and W. D. Robertson, "The Martensitic Transformation in Single Crystals of Iron-Chromium-Nickle Alloys", Acta Metallurgica, Vol. 10, Nov. 1962, pp. 1077-1088.

[18] G. W. Powell, E. R. Marshall and W. A. Backofen, "Strain Hardening of Austenitic Stainless Steel", Trans. ASM, Vol. 50, 1958, pp. 478-497.

[19] S. S. Hecker, M. G. Stout, K. P. Staudhammer and J. L. Smith, "Effects of Strain State and Strain Rate on Deformation-Induced Transformation in 304 Stainless Steel: Part I: Magnetic Measurements and Mechanical Behavior", Metall. Trans. A, 13A, April 1982, pp. 619-626.

[20] G. B. Olson and M. Cohen, "Kinetics of Strain-Induced Martensitic Nucleation", Metall. Trans. A, 6A, 1975, pp. 791-795.

[21] M. L. Holzworth and M. R. Louthan, Jr. , "Hydrogen-Induced Phase Transformations in Type 304L Stainless Steels", Corrosion, Vol. 24, No. 4, Apil, 1968, pp. 110-124.

[22] H. Hanninen and T. Hakarainen, "On the Effects of Alpha Prime Martensite in Hydrogen Embrittlement of a Cathodically Charged AISI Type 304 Austenitic Stainless Steel", Corrosion, Vol. 36, No. 1, Jan. 1980, pp. 47-51.

[23] M. R. Louthan, Jr., "Effects of Hydrogen on The Mechanical Properties of Low Carbon and Austenitic Steels", Hydrogen in Metals, I. M. Bernstein and A. W. Thompson, Eds., ASM, Metals Park, Ohio, 1974, pp. 53.

[24] A. J. Bursle and E. N. Pugh, 1977 TMS/AIME Fall Meeting, Chicago, Oct. 1977, pp. 24-27.

[25] A. J. West and J. H. Holbrook, "Hydrogen in Austenitic Stainless Steels: Effects of Phase Transformations and Stress State", Hydrogen Effects in Metals, I. M. Bernstein, A. W. Thompson, Eds., 1980, pp. 607-618.

[26] G. R. Caskey, Jr., "Hydrogen Effects in Stainless Steel", Hydrogen Degradation of Ferrous Alloys, R. A. Oriani, J. P. Hirth and M. Smialowski, Eds., 1985, pp. 822-862.

[27] G. R. Caskey, Jr. "Hydrogen Damage in Stainless Steel", Environmental Degradation of Engineering Materials, Virginia Polytechnic Institute, 1981, pp. 283-302.

[28] B. D. Cullity, Elements of X-ray Diffration, 2nd Edition.

[29] G. R. Caskey, Jr. "Fractography of Hydrogen-Embrittled Stainless Steel", Scripta Metallurgica, Vol. 11, 1977, pp. 1077-1083.

[30] M. Gao, Shuchun Chen and R. P. Wei, submitted to Metall. Trans. A, 1990.

[31] L. E. Murr, K. P. Staudhammer and S. S. Hecker, "Effects of Strain Rate on Deformation-Induced Transformation in 304 Stainless Steel: Part II. Microstructural Study", Metall. Trans. A, 13A, April 1982, pp. 627-635.

[32] H. Hanninen and T. Hakkarainen, "Fractographic Characteristics of a Hydrogen-Charged AISI 316 Type Austenitic Stainless Steel", Metall. Trans. A, 10A, August 1979, pp. 1196-1199.

VITA

Shuchun Chen was born on February 15, 1963 in Heilongjiang Province, the People's Republic of China. In 1981, he completed his high school education from Zhaoyuan First High School in Heilongjiang Province, China. In July 1985, he received his degree of Bachelor of Science in Physical Metallurgy from Dalian University of Technology (former Dalian Institute of Technology), Dalian, China.

In August 1985, Mr. Chen was admitted as a graduate student by Dalian University of Technology after he passed the National Graduate Entrance Examination of the year. Because of his outstanding academic achievement, he was awarded a scholarship for study in United States of America by the State Education Committee of China and the Li Foundation in New York. For this purpose, he was trained in an intensive English program at Beijing Institute of Foreign Languages in Beijing, China, from October 1985 to May 1986, and was issued a diploma. In May 1986, he took TOEFL examination in Beijing, China. In October 1986, he took GRE examinations both general and engineering subject in Dalian, China.

In September 1987, Mr. Chen started his graduate study under the guidance of Professor Robert P. Wei in Department of Materials Science and Engineering at Lehigh. His master's research involved the investigation of the effect of microstructure on corrosion fatigue of crack growth in AISI 304 stainless steels. Mr. Chen passed the Ph.D. qualifying examination of the Department of Materials Science and Engineering at Lehigh in May 1989. He will continue his education for the degree of Doctor of Philosophy in Materials Science and Engineering.

In November 1986, Mr. Chen was married to Miss Minxia Liu, formerly from Dalian City in China.